Polyclonal and single clonal patient-derived organoid models of Barrett oesophagus and oesophageal adenocarcinoma establish a platform for the analysis of heterogeneity in disease progression and therapy response

Daniel H Jacobson[1*], Dylan P McClurg[1*], Emily Black[1], Charlotte Cassie[1], Tik Shing Cheung[1], Hannah Coles[1], Ginny Devonshire[1], SriGanesh Jammula[1], Benjamin Hall[2], Xiaodun Li[1], Ahmad Miremadi[3], Krishnaa T Mahbubani[4], Massimiliano di Pietro[1], Kourosh Saeb-Parsy[4,5], Oesophageal Cancer Clinical and Molecular Stratification (OCCAMS) Consortium, Rebecca C Fitzgerald[1#], Christopher M Jones[1,3^] and Lizhe Zhuang[1^]

* These authors contributed equally.

^ These authors contributed equally.

[1] Early Cancer Institute, Department of Oncology, University of Cambridge, Cambridge, UK

[2] Department of Medical Physics & Biomedical Engineering, University College London, London, UK

[3] Addenbrooke's Hospital, Cambridge University Hospitals NHS Foundation Trust, Cambridge, UK

[4] Cambridge Biorepository for Translational Medicine (CBTM), NIHR Cambridge Biomedical Research Centre, Cambridge, UK

[5] Department of Surgery, University of Cambridge, Cambridge, UK

Address for correspondence: Professor Rebecca C. Fitzgerald
Early Cancer Institute
Department of Oncology
University of Cambridge
Cambridge Biomedical Campus
Cambridge, CB2 0XZ, UK

Email: rcf29@cam.ac.uk

HIGHLIGHTS

1. Patient- and healthy donor-derived organoids (PDOs) provide a functional platform of disease progression and heterogeneity across normal gastric, non-dysplastic and dysplastic Barrett oesophagus (BO) and oesophageal adenocarcinoma (OAC).
2. We provide a quantitative phenotypic and molecular framework to assess the provenance and fidelity of each PDO model given the heterogeneity of this disease.
3. PDOs recapitulate key features of non-dysplastic and dysplastic BO, as well as invasive OAC.
4. Single cell-derived clonal organoids (sc-organoids) isolate and maintain high-risk subclonal populations.
5. OAC PDOs mirror known population level variation in response to systemic anti-cancer therapies.

SUMMARY/ABSTRACT

Oesophageal adenocarcinoma (OAC) is a major cause of morbidity and mortality. OAC and its precursor, Barrett oesophagus (BO), are defined by substantial early heterogeneity, complicating prevention and treatment of OAC and remaining poorly recapitulated by current *in vitro* and animal model systems. We have generated 116 patient- and healthy donor- derived organoids (PDOs) spanning normal oesophagogastric tissue, BO and OAC. These PDOs capture population diversity and recapitulate phenotypic, genomic and transcriptomic features of their respective disease stages. We develop a single cell-derived clonal organoid approach and show that this enables us to capture the heterogeneity and isolate high-risk, subclonal populations that are difficult to discern and maintain in bulk PDO cultures. Using this platform, we demonstrate functional importance of this biobank across the pre-malignant to invasive disease spectrum, including a role for BO in shaping fibroblast phenotype within assembloids, and diverse responses of OAC to chemotherapy, radiotherapy and targeted CDK4/6 inhibition.

Key words: Barrett oesophagus; Dysplasia; Oesophageal adenocarcinoma; Organoid; Assembloid; Heterogeneity; Systemic anti-canccer therapy; Chemotherapy; Radiotherapy

INTRODUCTION

Oesophageal adenocarcinoma (OAC) is an important cause of cancer-related morbidity and mortality, with an overall five-year survival rate of less than 20%[1]. Around 85,000 people are diagnosed with OAC each year, corresponding to a global age-standardised incidence of 0.9 cases per 100,000 persons[2]. Following increases in incidence since the 1970s, OAC is now the dominant subtype in over 20 high income countries, where rates reach as high as 3.4 cases per 100,000 people[2, 3].

The development of OAC follows the replacement of the normal stratified oesophageal squamous epithelium with a metaplastic mosaic of gastric and intestinal like epithelium[4]. This lesion, Barrett oesophagus (BO), originates from cells within the gastric cardia, likely in response to exposure to injurious gastric refluxate[4, 5]. BO typified by intestinal metaplastic features can progress to dysplasia and invasive disease but this occurs in a minority of patients, with an annual risk of OAC of just 0.3% for a person with a non-dysplastic lesion[6]. Greater phenotypic and molecular variation also correlates with the risk of progression to OAC[7-9]. A more precise understanding of events leading to progression is vital to enabling early detection and interception strategies[10]. The heterogenous nature of the BO precursor lesion gives rise to a highly diverse cancer at phenotypic and molecular levels of resolution[11-13]. This tumour heterogeneity establishes a therapeutic landscape with few recurrent actionable drivers for targeted therapies and high levels of resistance to conventional treatments and immunotherapy, leading to poor outcomes[10, 14].

There is consequently a need to develop an experimental platform that recapitulates inter- and intra-lesional heterogeneity from the development of BO through to its dysplastic progression to OAC. In this context, animal models are poorly representative and do not reproduce between-patient heterogeneity[15]. The use of animal models is also costly and resource intensive, with multiple ethical implications that have prompted calls to move away from their routine use. By contrast, we have previously shown that OAC patient-derived organoids (PDOs) can be established[16]; however, the extent to which these also reproducibly demonstrate heterogeneity in therapeutic response to established therapies including cytotoxic chemotherapy and external beam radiotherapy (EBRT) is less certain[17, 18]. PDOs also lack stromal factors that are known to contribute to disease pathogenesis and treatment response, such as the presence of fibroblasts[19, 20]. Moreover, establishing these models from precancerous lesions has proven more challenging[16]. The aim of this study was therefore to establish and characterise a PDO biobank of

sufficient scale to recapitulate the full spectrum of heterogeneity at each stage of disease progression, including normal gastric epithelium, non-dysplastic and dysplastic BO, and treatment-naïve as well as treated OAC. Using a combination of genomic sequencing and *in silico* modelling of PDO growth and morphology, we provide a quantitative toolkit to characterise each organoid. To address intralesional heterogeneity in BO, we also introduce novel, single cell-derived clonal organoids (sc-organoids) to unmask minor cell populations at high risk of dysplastic progression that may be missed in bulk analyses or lost through successive passages. We show that co-culture with fibroblasts (termed assembloids) and microenvironmental stressors results in altered epithelial-fibroblast interactions and the reprogramming of stromal components. Finally, we demonstrate that OAC PDO phenotypic and molecular heterogeneity translates to variation between PDOs in their response to different forms of cytotoxic chemotherapy, EBRT and targeted therapy.

METHODS

Study approach and regulatory approval

Samples were obtained from surgical or endoscopic resection specimens obtained from patients with known BO, dysplasia or OAC (sampling and PDO biobank summarised in **Supplementary Figure 1)**. Prior ethical approval was provided by the United Kingdom Health Research Authority, including: “A study to investigate the cell biological determinants of the development and progression of the pre-malignant condition in Barrett's oesophagus” (Biomarker), 01/149; “Multicentre Study to determine predictive and prognostic biomarkers and therapeutic targets for oesophageal and junctional adenocarcinoma including whole genome sequencing” (OCCAMS), 10/H0305/1; “A study using tissue to develop stem cell-based therapies and to investigate human physiology, pathology and embryonic development” (Organ donor), 15/EE/0152. All patients provided written informed consent prior to sampling, which was performed within a National Health Service setting.

Sampling strategy

To derive non-dysplastic BO PDOs two to three biopsy specimens were taken from the same region at surveillance endoscopy, with a preference for adjacent sampling wherever possible. All dysplastic BO PDOs and a single OAC PDO were obtained from specimens taken via a punch biopsy from an endoscopic mucosal resection (EMR). For OAC models, resection specimens were evaluated and samples obtained for organoid derivation and adjacent tissue for snap freezing. For control gastric PDOs and intestinal PDOs, both patients and disease-free organ

69 donor tissues were used. Samples were briefly minced and mixed to ensure homogeneity, and
70 half or two thirds of the tissue mixture was immediately processed to derive PDOs, the methods
71 for which are outlined below. The remnant was snap-frozen using liquid nitrogen and stored at -
72 80°C for profiling of adjacent tissues recognising that given the heterogeneity there will be
73 potential differences at the cell and molecular level. To further mitigate and understand the
74 genotype to phenotype correlation in all cases, a section was cut from each snap frozen sample
75 and stained with haematoxylin and eosin (H&E) prior to DNA extraction. The H&E-stained slide
76 was independently reviewed by at least two experienced pathologists to assess cellularity, and
77 to confirm malignancy for OAC or to assess for the presence and severity of dysplasia in BO. In all
78 instances, only samples with at least 70% cellularity were used for deoxyribonucleic acid (DNA)
79 or ribonucleic acid (RNA) extraction using the AllPrep kit (Qiagen). DNA was extracted from blood
80 samples using the QIAmp DNA Blood Maxi kit (Qiagen). In all cases a germline reference was
81 obtained from blood wherever possible or otherwise from distant normal mucosa.
82
83 **Derivation of BO PDOs**
84 To derive BO PDOs, biopsy samples were rinsed in ice-cold phosphate buffered saline (PBS) and
85 pooled. These were then minced and digested using recombinant TrypLE Express Enzyme
86 (ThermoFisher) supplemented with 10μM Y-27632 (Tocris Bioscience) at 37°C for up to 10
87 minutes. Vigorous shaking was used every three minutes to dissociate tissue aggregates. Cells
88 were pelleted at 300g for 5 minutes and resuspended in 150μl TrpLE Express Enzyme. Further
89 mechanical dissociation was achieved using a P200 pipette prior to centrifugation at 300g for 5
90 minutes. The resultant single cell mixture was resuspended in Cultrex Basement Membrane
91 Extract (BME) Type 2 (R&D Systems) and plated as 15μl domes for ongoing culture.
92
93 **Derivation of OAC PDOs**
94 Samples obtained from surgical resection specimens were processed as per our previously
95 reported protocol[16]. Briefly, each sample was rinsed in ice-cold PBS, minced then digested
96 through incubation at 37°C with collagenase II (1.5mg/ml) for up to 2 hours. Large fragments were
97 then removed by filtration using a 70μM cell strainer and the resultant cell suspension centrifuged
98 at 400g for 2 minutes. The pellet was resuspended in PBS as a further wash step to remove debris
99 and a further identical centrifugation step performed. Isolated cells were then resuspended in
100 Cultrex BME Type 2 and plated as 15μl-20μl domes for ongoing culture.
101
102 **Derivation of gastric and intestinal PDOs**

103 Gastric PDOs were established either from endoscopic biopsies of the gastric cardia from BO
104 patients or from gastroesophageal junction (GOJ) tissue from disease-free organ donors. For
105 gastric cardia PDOs derived from BO patients, biopsy specimens were processed using the same
106 protocol as for BO PDO derivation. Gastric PDOs from organ donors were generated as described
107 in our previous study[5] . Briefly, a circumferential tissue fragment (up to 10 cm in length) spanning
108 3–5 cm of distal oesophagus and 3–5 cm of proximal stomach was obtained. GOJ PDOs were
109 established from a 5 mm tissue strip spanning the Z-line (squamous–columnar junction). Gastric
110 body PDOs were derived from tissue located at least 2 cm below the Z-line. Intestinal PDOs were
111 kindly provided by Professor Fiona Gribble, University of Cambridge. In brief, intestinal organoids
112 were generated from healthy jejunal or duodenal tissue obtained from patients undergoing
113 gastrectomy or pancreaticoduodenectomy **(Supplementary Table 2)**. Note: although organ-
114 donor-derived organoids are not strictly patient-derived, we refer to them as PDOs for
115 consistency and ease of interpretation throughout the manuscript.
116
117 **PDO culture**
118 All PDO cultures were maintained in a humidified atmosphere with 5% carbon dioxide (CO_2) at
119 37°C. PDOs were maintained in IntestiCult™ Organoid Growth Medium (StemCell Technologies)
120 supplemented with Primocin (1mg/ml, InvivoGen) and Y-27632 (10μM), with or without FGF10
121 (100ng/ml, Peprotech) and Gastrin (10nM, Sigma). Media was refreshed every two to five days for
122 cell maintenance outside of specific experimental conditions. PDOs were passaged at least
123 every two weeks through the addition of pre-warmed TypLE Express Enzyme and manual
124 dissociation by pipetting. The resultant cell solution was centrifuged at 300g for 5 minutes,
125 providing a cell pellet that was resuspended in Cultrex Basement Membrane Extract, Type 2 and
126 plated as 15μl-20μl domes that were allowed to polymerise prior to the addition of media. Once
127 established, BO and intestinal PDO cultures were maintained in organoid medium (OWR)
128 prepared from Advanced Dulbecco's Modified Eagle Medium (DMEM)/F-12 supplemented with
129 0.5nM Wnt Surrogate-Fc Fusion Protein (N001, U-Protein Express BV), 9.6nM RSPO3-Fc Fusion
130 Protein conditioned medium (R001, U-Protein Express), 10mM HEPES, 1× Glutamax, 1× N2,
131 100ng/mL Noggin, 10 mM Nicotinamide, 1 mM N-acetylcysteine, 1×B27, 50ng/mL EGF, 500nM
132 A8301, 10μM SB202190, 1× Primocin, 10nM Gastrin, 10μM Y-27632 and 100ng/mL FGF10.
133
134 **Establishment of single cell-derived clonal organoids**
135 To isolate specific clonal populations, we cultured PDOs to around 70-80% confluency in Cultrex
136 BME Type 2 domes. Culture medium was then removed and replaced with an ice-cold mixture

137 comprising of a 1:1 ratio of TrypLE Express Enzyme and Advanced Dulbecco's Modified Eagle
138 Medium (DMEM)/F-12 supplemented with 10μM Y27632 (TrypLE/ADF). A P1000 pipette was then
139 used to manually break the BME Type 2 domes whilst leaving PDOs intact. The resultant mixture
140 was transferred to the underside of a sterile Corning cell culture plate lid with multiple 40μl
141 TrypLE/ADF droplets. Using a brightfield microscope, the PDO suspension was inspected for
142 single organoids exceeding a diameter of 200μm. Once identified, these were aspirated under
143 direct vision using a P20 pipette and transferred to a TrypLE/ADF droplet. This process was
144 repeated multiple times and each droplet then transferred to a fresh 1.5ml microcentrifuge tube.
145 This was incubated at 37°C for five minutes using a ThermoMixer® (Eppendorf). A P20 was then
146 used to mechanically dissociate the isolated PDO and the resultant single cell solution
147 resuspended in Cultrex BME Type 2 and plated as 15μl domes for ongoing culture. Of note, to
148 study heterogeneity in BO and dysplasia, single organoids were picked from passage 0 cultures,
149 i.e. cultures established directly from tissue without any passaging, to ensure that distinct clonal
150 populations were selected.
151
152 **Establishment of assembloid co-cultures**
153 Primary human oesophageal fibroblasts (ABM-T4232, Applied Biological Materials), were a gift
154 from Professor Jacqueline Shields, University of Nottingham. Fibroblasts were maintained in
155 Fibroblast Medium (SC-2301, Caltag Medsystems Ltd). Organoids were harvested, resuspended,
156 and mixed with fibroblasts at a 1:2 ratio in OWR medium supplemented with 5% foetal bovine
157 serum (FBS) and 10% Cultrex BME Type 2, and seeded into round-bottom 96 well plates. Each
158 well contained 100μL with 225,000 cells. Plates were centrifuged at 300g for 5 minutes to pellet
159 cells and then incubated at 37°C overnight. During this period, the cells self-assembled into a
160 sphere, which was subsequently transferred into a Cultrex BME Type 2 dome in a 48 well plate as
161 assembloids and maintained in OWR medium for 7 days.
162
163 To explore microenvironmental influences, assembloids were treated for 7 days with either 5 mM
164 refluxate salt (sodium glycocholate hydrate; Sigma), 10 ng/mL IL10 (R&D Systems), or a
165 combination of both. For conditions containing refluxate salt, assembloids were exposed to the
166 treatment for only 6 hours per day. Assembloids from each treatment condition were dissociated
167 into a single cell suspension and stained with LIVE/DEAD™ Fixable Violet (1:1000, Thermo Fisher
168 Scientific). For detection of human-specific markers, the following antibodies were used: anti-
169 EpCAM (APC, clone 9C4, BioLegend), anti-α-SMA (PE, clone 1A4, R&D Systems), and anti-CD34
170 (BV510, clone 581, BioLegend). Intracellular staining was performed as outlined previously[21].

171 Briefly, cells were fixed using the Cytofix/Cytoperm Fixation and Permeabilization Solution (BD
172 Biosciences, UK) and permeabilized with 1x permeabilization buffer (Thermo Fisher Scientific,
173 UK). Positive staining was assessed relative to fluorescence-minus-one (FMO) controls. Doublets
174 and dead cells were excluded during analysis. Fibroblasts within the assembloids were gated
175 from the EpCAM-negative population. Data were acquired on an LSRFortessa (BD Biosciences)
176 and analysed using FlowJo software (Freestar Inc).
177
178 **PDO treatment using systemic anti-cancer therapies**
179 The viability of OAC PDOs was assessed following exposure to individual components of FLOT (all
180 supplied by SelleckChem) and to the cell cycle inhibitor, abemaciclib (LKT labs). To mirror clinical
181 administration, oxaliplatin and docetaxel were administered to PDOs as single agents whereas
182 5-fluorouracil was administered in combination with a fixed dose of leucovorin. Each drug was
183 reconstituted as per manufacturer instructions and each was diluted in either DMSO (5-
184 fluorouracil, docetaxel, and abemaciclib) or ultrapure water (oxaliplatin and leucovorin) to values
185 within a range of 200μM-0.195μM for components of FLOT, except for leucovorin, which was
186 administered at 10μM on all occasions, and 0.001-10μM for abemaciclib. Values for both dilution
187 series were selected based on others reported in the literature[22, 23]. The concentration of DMSO
188 was fixed at ≤0.1% within treatment and control vehicle wells.
189
190 In line with existing protocols, PDOs were dissociated using TrypLE Express Enzyme then counted
191 and resuspended in BME Type 2 prior to drug exposure[16, 24]. A total of 5000 cells were seeded
192 within 20μL BME Type 2 droplets formed at the centre of each well of a 96-well plate. These were
193 allowed to polymerise prior to the addition of media. Cultures were maintained for 72 hours and
194 then exposed to drug when in a logarithmic growth stage. Viability was assessed after 144 hours
195 exposure to components of FLOT, abemaciclib, or vehicle. Media, including drug or vehicle, was
196 refreshed after 72 hours for PDOs treated with FLOT constituent drugs.
197
198 **PDO treatment using external beam radiotherapy**
199 Prior to irradiation, established PDOs were dissociated to a single cell solution. This was
200 performed by first dissociating PDOs from Cultrex Basement Membrane Extract, Type 2, through
201 incubation with pre-warmed TypLE Express Enzyme and manual agitation by pipetting.
202 Dissociated PDOs were pelleted by centrifugation at 300g for 5 minutes and resuspended in 30μl
203 cool PBS. A P20 pipette was then used to manually dissociate the PDOs to a single cell solution
204 and the cell concentration assessed using a Countess II Automated Cell Counter (Invitrogen). A

205 total of 10,000 cells were plated in 15µl Cultrex Basement Membrane Extract, Type 2 with media
206 added once this had polymerised. The media was replaced with pre-warmed PBS prior to
207 irradiation 24 hours later using a CIX1 (XStrahl) benchtop irradiator. Single fraction treatments of
208 0Gy (sham), 2Gy, 4Gy, 6Gy and 8Gy x-ray irradiation were delivered and PBS then replaced with
209 media 15 minutes after irradiation.
210
211 **Whole genome sequencing**
212 Extracted DNA was subjected to paired-end whole genome sequencing at a depth of 50x for
213 tissues, 30x for PDOs and 15x for sc-organoids, using a well-established pipeline[11]. A
214 combination of in-house tools and FastQC
215 (http://www.bioinformatics.babraham.ac.uk/projects/fastqc) were used for quality control.
216 Sequencing reads were aligned against the hg19/Ensembl GRCh38 reference genome for
217 mutation calling using the Burrows-Wheeler BWA-MEM alignment algorithm[25]. Aligned reads
218 were subsequently sorted into genome coordinate order and Picard
219 (http://broadinstitute.github.io/picard) used to remove duplicate reads. Single nucleotide
220 variants and insertion deletion mutaitons were called with Strelka v2.0.15[26]. Tumour purity and
221 ploidy were inferred with ASCAT-NGS v2.17, and copy number alterations derived with ASCAT
222 from read counts at germline heterozygous sites identified by GATK HaplotypeCaller v3.2-2,
223 adjusting for the estimated normal-cell component. Structural variants (SVs) were called using
224 MANTA v0.27 with any SVs that had any supporting reads in the matched normal being discarded
225 as previously described[27].
226
227 **RNA sequencing**
228 Extracted RNA was quality assessed using the RNA 6000 Nano Kit (Agilent) on a 2100 Bioanalyser
229 (Agilent). Samples for which there was sufficient material available for further analysis and that
230 had a calculable RNA integrity number were determined to have passed quality control and were
231 quantified using the Qubit High sensitivity RNA assay kit (Thermo Fisher). The TruSeq Stranded
232 Total RNA High Sensitivity protocol with ribosomal depletion was used to prepare libraries using
233 an input of at least 100ng but preferably 250ng if available. KAPA quantification (KAPA
234 Biosystems) was used to quantify libraries, which were pooled and run on a HiSeq 4000 to
235 generate 75 base pair adjacent-end reads. After sequencing, reads were aligned by STAR. Gene-
236 level counts for each sample were generated using Bioconductor's GenomicAlignments package
237 together with ENSEMBL gene annotations. These raw counts, along with sample-specific

238 sequencing depths and gene lengths, were then used to calculate Transcripts Per Kilobase Million
239 (TPM) values for individual genes across all samples.
240
241 **Bioinformatic analyses**
242 In determining relevant driver events, we considered mutations in 76 genes identified by Frankell
243 et al. as positively selected for in OAC[11]. Amplification events were defined as cases where copy
244 number was more than double the sample ploidy, whilst deletion events were strictly defined as
245 a total copy number of zero. Losses in the single cell-derived clonal organoids were defined as a
246 minor copy number of zero. Two PDOs (OESO/117 and OESO/146) were used for chemotherapy
247 treatment screens but underwent WGS elsewhere. Clinical and genomic information for these
248 PDOs was obtained from Cell Model Passports (https://cellmodelpassports.sanger.ac.uk/).
249
250 The HRD index score, the sum of three HRD-associated copy number features applied here as a
251 broad measure of total chromosomal instability, was calculated using the scarHRD R package[28,
252 29]. Mutational signatures were extracted de novo using SigProfiler applied to the complete set of
253 OAC tissues and PDOs, resulting in the following signatures: SBS1, SBS2, SBS5, SBS8, SBS13,
254 SBS17a, SBS17b, SBS18, SBS31, SBS35, SBS40, SBS93[30]. These signatures were then fitted using
255 the deconstructSigs R package with a 2% prevalence cut-off[31]. Signatures SBS31 and SBS35 were
256 not fitted for BO PDOs since they are caused by platinum chemotherapy. Subclonal
257 reconstruction of the non-dysplastic BO PDOs was conducted with PyClone-VI using the beta-
258 binomial distribution[32].
259
260 Phylogenetic analysis of the single cell-derived clonal organoids was conducted using the
261 parsimony ratchet method as implemented through the phangorn R package[33], with branch
262 lengths assigned according to the ACCTRAN criteria. Specific SNVs were assigned to branches
263 onto which they fitted exactly based on their presence across organoids deriving from the
264 respective branch. A subset of the above signatures (SBS1, SBS2, SBS5, SBS8, SBS13, SBS17a,
265 SBS17b, SBS18, SBS40) with established presence in BO, and that do not relate to chemotherapy
266 treatment, were fitted using deconstructSigs to any branch with more than 25 unique SNVs.
267 Barplots for signature contributions were plotted onto the corresponding branch and extended
268 manually to fit the branch length.
269
270 Differential gene expression analysis was conducted using the DESeq2 R package[34]. Functional
271 enrichment of differentially expressed gene sets was analysed using the gProfiler2 R package[35],

272 specifically on genes with p-value (false discovery rate adjusted for multiple testing) of less than
273 0.05 and with an absolute log2-fold change greater than 1, and separated into up- and down-
274 regulated genes. This package enables enrichment analysis against multiple databases including
275 Gene Ontology, the Human Protein Atlas for cell-type analysis, and TRANSFAC for transcription
276 factor-binding profiles. Gastric and intestinal gene set 'scores' were calculated through gene set
277 variation analysis of the TPM-normalised data, using the GSVA R package[36], taking *MUC6*,
278 *MUC5AC*, *CLDN18*, *PGC*, *GKN1*, *GKN2* as gastric genes and *MUC2*, *TFF3*, *REG4*, *GPA33*, *CDX2*,
279 *FABP2*, *OLFM4*, *ANPEP* as intestinal genes.
280
281 RNA-seq counts for OAC-derived PDOs underwent batch correction using ComBat, as part of the
282 sva R package[37]. Principal component analysis was conducted on the top 1000 variable genes
283 following batch correction and variance stabilising transformation. Gene set enrichment
284 analysis, using the cancer hallmark gene sets, was applied on the loadings of each gene for the
285 first two principal components using fgsea. Normal gastric, normal intestinal, and BO-derived
286 PDOs were sequenced in the same batch and so correction was not required.
287
288 **Organoid forming efficiency assay**
289 All PDOs were imaged on the day of, and 10-days following, irradiation using an Incucyte® SX5
290 Live-Cell Analysis System (Sartorius, Goettingen, Germany). The Incucyte® Organoid Analysis
291 Module (Sartorius, Goettingen, Germany) was used to count the number of PDOs at each
292 assessed timepoint using a segmentation radius of 100µm, segmentation sensitivity of 30,
293 segmentation edge split with sensitivity of 100, cleanup with hole fill of 500,000µm^2 and an
294 adjusted pixel size of -1. Filters were set to count objects as PDOs only with a minimum area of
295 1500µm^2 and maximum eccentricity of 0.25 as a strict cut-off to exclude budding, migrating or
296 necrotic PDOs. Given that there should not be PDOs formed at day zero, the PDO count at this
297 point was considered to reflect noise and was subtracted from the day 10 PDO count. Organoid
298 formation efficiency was calculated for each radiation dose as the number of formed PDOs at
299 day 10 divided by the cell seeding number, 10,000. Relative organoid forming efficiency was
300 determined by dividing the organoid forming efficiency at each delivered dose by the organoid
301 forming efficiency at 0Gy.
302
303 **PDO viability**
304 PDO viability was quantified using a luminescent assay 72- or 144- hours after respective
305 administration of abemaciclib or FLOT. In accordance with manufacturer instructions, 20uL of

306 CellTiter-Glo® 3D (Promega) was applied to each well of a 96-well plate, which was then shaken
307 for five minutes. Plates were then incubated for 30 minutes in a humidified atmosphere with 5%
308 CO_2 and luminescence read using an Infinite 200 Pro microplate reader (Tecan).
309
310 **PDO fluorescent labelling**
311 PDOs derived from BO and OAC were labelled with fluorescent nuclear markers via lentiviral
312 transduction. Briefly, PGK-H2B-eGFP or PGK-H2B-mCherry plasmids were co-transfected with
313 pMD2.G and psPAX2 into HEK293 cells (a gift from Sakari Vanharanta, University of Helsinki) to
314 produce lentivirus, following the protocol described in Kita-Matsuo et al[38]. Viral supernatant was
315 concentrated 16-fold using the Lenti-X™ Concentrator (631231, Takara Bio) and resuspended in
316 organoid medium. Organoids were harvested, resuspended in 15 µL (approximately 500,000
317 cells), mixed with 250 µL of concentrated lentivirus, and incubated for 4 hours at 37 °C. The
318 organoids were then washed, seeded, and maintained under standard culture conditions.
319
320 PGK-H2BeGFP was a gift from Mark Mercola (Addgene plasmid # 21210;
321 http://n2t.net/addgene:21210; RRID: Addgene_21210). PGK-H2BmCherry was a gift from Mark
322 Mercola (Addgene plasmid # 21217; http://n2t.net/addgene:21217; RRID: Addgene_21217).
323 pMD2.G was a gift from Didier Trono (Addgene plasmid # 12259; http://n2t.net/addgene:12259;
324 RRID: Addgene_12259). psPAX2 was a gift from Didier Trono (Addgene plasmid # 12260;
325 http://n2t.net/addgene:12260; RRID: Addgene_12260).
326
327 **Fluorescent in situ hybridisation**
328 Flourescent *in situ* hybridisation (FISH) was performed using routine diagnostic *HER2* probes. As
329 previously described[39], PDO cultures were prepared using standard cytogenic procedures for
330 harvesting, fixation (3:1 methanol : acetic acid solution) and slide formation. All subsequent pre-
331 treatment and hybridisation steps were undertaken in accordance with manufacturer
332 instructions by the Department of Histopathology, Cambridge University Hospitals NHS
333 Foundation Trust.
334
335 **Time-lapse imaging of PDO growth and morphology**
336 Time lapse imaging was performed using a Zeiss Axio Observer Live Cell Station at 10x
337 magnification at either 2-4 hourly intervals or at day 4, 6 and 7 after single cell seeding. Up to four
338 locations were imaged at each time interval with images captured across up to 23 slices through
339 a z-stack of the Cultrex BME Type 2 dome in which the PDOs are cultured. Brightfield images were

acquired, in addition to GFP fluorescence via excitation at 469nm with emission recorded at 525nm using a GFP filter set, and mCherry fluorescence via excitation at 590nm with emission at 687nm using an mCherry filter set. Exposure time and acquisition parameters were kept constant at all imaging intervals. Images were processed using Zeiss Zen software.

Computational analyses of PDO growth kinetics and morphology

Once processed, images of PDOs obtained at each timepoint were analysed using the Fiji distribution of ImageJ[40, 41]. Given an inherent partial eccentricity, each PDO was manually delineated using an ellipse. The minimum and maximum widths of this were averaged to give an approximate value for the PDO diameter. Though often visible across multiple levels of a z-stack, PDOs were measured only once, at the plane at which they were most in focus. PDOs were simultaneously categorised by morphology and distinguished by the presence or absence of a visible lumen, which if present was categorised as single or multiple, and whether the cells surrounding the lumen were a single cell layer or of multiple layers. For hollow PDOs (i.e. those with a lumen), the number of cells within that PDO was presumed to be proportional to the square of the diameter (i.e. the surface area). For solid organoids (i.e. those lacking a lumen), the number of cells in that PDO was presumed to be proportional to the cube of the PDO (i.e. the volume of the organoid).

An *in silico* cell-level model of PDO growth was built in CompuCell3D (CC3D) Version 4.2.5[42]. This implements a lattice-based multi-site Cellular Potts Monte Carlo model and has previously been used to model cells growing around a lumen. Briefly, each cell in this model can occupy a number of lattice sites. A model is developed to minimise the energy of the lattice conformation using the following equation:

$$E = \sum_{\vec{i},\vec{j}} J\left(\tau\left(\sigma(\vec{i})\right), \tau\left(\sigma(\vec{j})\right)\right)\left(1 - \delta\left(\sigma(\vec{i}), \sigma(\vec{j})\right)\right) + \sum_{\sigma} \lambda_{vol}(\sigma)\left(v(\sigma) - V_t(\sigma)\right)^2$$

where the first sum represents energy changes due to cell adhesion for every pair of neighbour lattice sites (*i, j)* and the second sum represents volume constraints for every cell, σ. In the first sum, *J* represents different adhesion energies between each pair of cell types $\tau\left(\sigma(\vec{i})\right)$ and $\tau\left(\sigma(\vec{j})\right)$, or between a cell type and the extracellular matrix. In the second equation, each cell has a target volume $V_t(\sigma)$ and a current volume $v(\sigma)$. The energy equation penalises deviation from the target volume, with $\lambda_{vol}(\sigma)$ representing cell elasticity. Multiple Monte Carlo Steps occur, with each considered a time unit proportional to experimental time. At each step each pixel will

attempt to copy itself to a neighbouring lattice site. This will succeed with probability 1 if the change reduces the overall energy, E, in the system.

The model was implemented in two dimensions, representing experimentally captured images of PDOs in cross section. Three cell types were used: polar, non-polar and lumen. Each lumen was modelled as a single 'cell', with the size of this lumen 'cell' determined by the number and type of cells surrounding the lumen.

Statistical analysis and reproducibility

All experiments were undertaken in at least biological triplicate unless otherwise stated. Given the known challenges of inter-batch heterogeneity in Cultrex BME Type 2 (R&D Systems), all biological replicates for irradiation experiments were performed using the same batch of BME Type 2. Integral area under the curve (AUC) values for organoid forming efficiency following irradiation were calculated using GraphPad Prism Version 10.4.1. for Windows (GraphPad Software, Boston, USA). Percent viability following exposure to systemic anti-cancer therapy was normalised to vehicle control and modelled against drug concentration using a three-parameter logistic (3PL) curve in GraphPad Prism v10.4.1 with Top fixed at 100%, and Bottom and Hill slope free. A four-parameter logistic (4PL) was also fit and retained only if it was clearly supported by the Akaike Information Criterion with small-sample correction (AICc) ($\Delta AICc \leq -4$) and the top 95% confidence interval excluded 100% across biological replicates; otherwise 3PL was used. Emax is reported as 100 − Bottom and the area under the curve (AUC) was computed over the tested log-dose range and normalised and reported as 1-AUC. Pairwise comparisons were made using the Mann-Whitney U test unless otherwise stated. Comparisons of more than two groups were made using the Kruskal Wallis test unless otherwise stated. Adjustments for multiple significance testing were made using the Bonferroni test unless otherwise stated in instances in which repeated statistical comparisons were drawn from the same dataset.

Data availability

Metadata to correlate information within this archive to that published here is provided in **Supplementary Table 1**.

Code availability

The scripts developed during the analysis presented here are available at the following GitHub repository, released under a GNU GPL-v3.0 license: https://github.com/fitzgerald-lab/OAC_Barretts_PDOprofiling. This includes scripts for analysing WGS data (e.g. driver gene

408 profiles, mutational concordance, signature contributions, phylogenetic analysis, clonal
409 dynamic analysis) and RNA-seq data (differential expression, unsupervised clustering, pathway
410 and gene-set analysis) obtained from BO, normal tissue-, and OAC-derived PDOs, and sc-
411 organoids.
412
413 **RESULTS**
414 **Establishment of PDOs spanning BO and healthy comparison tissues**
415 The first aim was to develop a robust and representative PDO resource spanning the entire
416 spectrum of BO development and progression prior to OAC development. Thirteen PDOs were
417 derived from non-dysplastic BO segments at routine surveillance endoscopy and eight PDOs
418 were derived from punch biopsies from regions of dysplasia in endoscopic mucosal resection
419 specimens **(Table 1)**. Respective efficiencies for deriving PDOs were therefore 68% (13/18) and
420 61% (8/13) from non-dysplastic and dysplastic tissue. In addition,16 normal gastric PDOs were
421 established, including seven from deceased healthy organ gastroesophageal squamocolumnar
422 junction (n=4) and gastric body (n=3) donor tissues **(Supplementary Table 2)**. Nine further gastric
423 PDOs were derived from patients with BO: one each from the gastric body and antrum, and seven
424 from the cardia to give a range of gastric lineages. Three further PDOs were derived from normal
425 intestinal tissue as control for the intestinal phenotype, which characterises BO with malignant
426 potential. All PDOs were passaged at least five times, and all were successfully revived following
427 cryopreservation.
428
429 **BO PDOs recapitulate population heterogeneity and key features of non-dysplastic as well**
430 **as dysplastic disease**
431 We first sought to understand the genomic heterogeneity of the BO PDOs in relation to dysplasia
432 status and in comparison to matching tissue samples. Median somatic mutation burden was
433 comparable and reflected disease stage, with 2.11 muts/Mb in non-dysplastic PDOs versus 1.89
434 muts/Mb in matching tissues, and 5.76 muts/Mb in dysplastic PDOs versus 4.57 muts/Mb in
435 matching tissues. Median burden in normal stomach was 0.11muts/Mb and 0.26 muts/Mb from
436 healthy- and patient- derived PDOs respectively **(Supplementary Figure 2, A and B)**. As
437 expected, PDOs showed higher purity, defined as the proportion of epithelial, precancerous
438 cells in a sample, and higher clonality than their matching tissues, which was achieved in non-
439 dysplastic and dysplastic models **(Supplementary Figure 2, C and D)**.
440

441 A comprehensive overview of OAC driver genes, mutational signatures, and clinical annotations
442 is provided in **Figure 1A**. As expected, there were few mutational events in normal gastric PDOs.
443 In contrast, *CDKN2A* alterations, primarily deletions, were identified in 31% of non-dysplastic
444 and 38% of dysplastic PDOs, consistent with the reported role of this gene in early BO
445 development[43]. Alterations in *TP53* were seen in only one (1/13, 8%) non-dysplastic BO PDO but
446 were more frequent (n=3/8; 37.5%) in PDOs taken from patients with dysplasia.
447
448 The fraction of shared mutations between BO PDOs and their matching tissues ranged from 0.3-
449 65.3% **(Figure 1B)**. Broadly, the mean fraction of private mutations (i.e. that are not shared) in
450 PDOs was higher in dysplastic PDOs than in non-dysplastic PDOs (median 56.9% vs 38.1%).
451 Whilst there was no correlation between the total number of insertion/deletion mutations in
452 PDOs and matching tissue (r=0.034, p=0.89), there was a moderate correlation in single
453 nucleotide variant (SNV) count (r=0.66, p=0.0015; **Figure 1C**) which was stronger for non-
454 dysplastic PDO/tissue pairs (r=0%.91, $p=3.4x10^{-5}$) **(Supplementary Figure 2E)**. These results
455 suggest increasing heterogeneity in dysplastic compared with non-dysplastic tissues which is
456 thus reflected in the variation captured within a given PDO model.
457
458 Most tissues and PDOs were diploid; however, we were keen to capture the whole genome
459 doubling observed in up to 27% high-grade dysplastic BO tissues[44]. Three PDOs had whole
460 genome doubling. This was mirrored in matching tissue for one PDO (AHM0931) but not in the
461 other two (AHM2575 (non-dysplastic) and AHM2165 (dysplastic), which featured whole genome
462 duplications despite diploid matching tissues **(Figure 1D)**. Overall concordance in homologous
463 recombination deficiency (HRD) index scores was low (r=0.15, p=0.53); however, again non-
464 dysplastic pairs showed a moderate positive correlation (r=0.52, p=0.081), though dysplastic
465 pairs did not (r=–0.34, p=0.41). This suggests that it is challenging to capture chromosomal
466 instability in PDOs and one cannot rely on the genomic profile of matching tissues
467 **(Supplementary Figure 2F)**.
468
469 In comparison to the accumulation of driver gene mutations, mutational signatures are laid down
470 early in the pathogenesis of BO and maintained consistently through malignant progression[45]. It
471 was therefore expected to observe a high concordance of mutational signatures in the PDOs and
472 matching tissues, with a median cosine similarity of 0.97 (range 0.73-1.00), which did not differ
473 between dysplastic and non-dysplastic PDO-tissue pairs **(Figure 1E and Supplementary Figure**
474 **2, G and H).** In particular, single base substitution signature 17 (SBS17a/b), a characteristic

475 feature of BO and OAC, showed a strong overall correlation for both SBS17a (r=0.83, p=6.2x10^{-6})
476 and SBS17b (r=0.88, p=3.8x10^{-7}) **(Figure 1F, Supplementary Figure 2I)**. As expected, SBS17a/b
477 proportions were similar across non-dysplastic and dysplastic PDOs **(Supplementary Figure 2J)**.
478
479 We also observed clonal heterogeneity and drift in precancerous PDOs **(Supplementary Figure**
480 **2, K and L).** For example, AHM0040 contained a major subclonal population (VAF 18%)
481 harbouring *ARID1A* and *FBXW7* driver mutations. In AHM1373, a subclonal cluster (median VAF
482 ~19%) was present at passage 1 but became clonal by passage 6 (median VAF 50%). Whilst no
483 driver alterations were present in both passages, passage 1 harboured a mutation in *LRKK2*
484 **(Figure 1A**), whilst passage 6 carried frameshift variants in *ARID1A*, *ARID1B*, and *MUC6*, possibly
485 indicating selection of a separate, rarer subclone. Hence, these models evolve temporally, and
486 this can be tracked genetically as required for their utility to study disease progression and
487 interception.
488
489 **Single cell-derived BO PDOs recapitulate intralesional heterogeneity**
490 In view of the substantial genomic heterogeneity and the passage-related clonal drift we
491 identified in BO PDOs, we reasoned that isolating low-frequency, high-risk populations would
492 enable single clone modelling of progression. To achieve this, we developed a microdissection
493 method to derive individual organoids from bulk PDO culture. We termed these single cell-
494 derived clonal organoids (sc-organoids) **(Figure 2A).**
495
496 We first generated 19 sc-organoids from a non-dysplastic case (AHM2149) and confirmed their
497 clonality by analysing VAF distributions (a narrow peak at 50% indicates clonality) **(Figure 2B)**.
498 The sc-organoid panel recapitulated key genomic features of matching BO tissue as well as the
499 related bulk PDOs, including deletions of *CDKN2A* and *KDM6A,* and mutations in *MUC6* and
500 *ZFHX3* **(Figure 2C)**. Interestingly, one sc-organoid, BE.11, harboured mutations in *TP53* and
501 *SMARCA4* that were not observed in the bulk PDO nor its matching tissue, suggesting a potential
502 "seed" for dysplastic progression. All sc-organoids contain private mutations (3.44%-45.8%),
503 confirming that each represents a distinct lineage with preserved mutational signatures
504 **(Supplementary Figure 3, A and B)**.
505
506 We next assessed the relatedness of the sc-organoids by constructing a phylogenetic tree using
507 WGS data **(Figure 2D)**. Most mutations (85.98%) fitted the tree perfectly with minimal homoplasy,
508 and driver alterations showed good concordance within the branching structure, reflecting their

individual acquisition along the evolutionary trajectory. For example, *FBXW7* loss was shared by BE.7 and BE.15 but absent in the bulk PDO, whereas a *ZFHX3* mutation was detected in the bulk PDO but found in only four closely related sc-organoids.

To determine whether closely related sc-organoids also display phenotypic similarity, we compared transcriptomic concordance with WGS-inferred phylogenies (**Figure 2E**). We also assessed whether sc-organoids represent distinct lineages by analysing enrichment of individual lineage markers (*MUC6* versus *CDX2*) and lineage gene panels (described in **Figure 3A**). Across 19 non-dysplastic BO sc-organoids, *MUC6* (gastric) and *CDX2* (intestinal) expression were strongly negatively correlated ($r = -0.71$; $p = 0.00075$, **Supplementary Figure 3C**), indicating that individual sc-organoids tend to adopt either a gastric or intestinal state. Notably, two sc-organoids (BO.8 and BO.23) displayed diverging transcriptional profiles to the rest of the sc-organoids, with significantly higher *CDX2* expression.

With these encouraging data we generated a panel of nine sc-organoids from dysplasia tissue from an early cancer case (AHM2392), from which a bulk PDO shared only 8.15% of SNVs and indels **(Figure 1B),** to better understand and model the clonal heterogeneity. All sc-organoids appeared clonal, with the exception of one (BE.14) that also harboured a nonsense mutation in *APC* present at a VAF of 25% **(Supplementary Figure 4A),** suggesting it may be a mixture of two clones. Taken together these sc-organoids shared a large proportion of mutations with the matching bulk PDO **(Supplementary Figure 4B)**, whilst also presenting with more mutations than the bulk PDO on account of their high clonality **(Supplementary Figure 4C)**. The individual sc-organoids nevertheless demonstrated clonal diversity **(Supplementary Figure 4D)** and transcriptomic heterogeneity **(Supplementary Figure 4E)**, which with the isolation of an *APC*-mutant clone reaffirms the potential for this technique to isolate high-risk populations not captured in bulk PDOs **(Supplementary Figure 4F)**.

***In silico* imaging reveals varying morphology, growth kinetics and between non-dysplastic and dysplastic BO PDOs**

The genomic profile must be interpreted in the context of PDO morphology and growth patterns to understand how this translates to phenotype. To assess morphology we genetically engineered non-dysplastic (AHM0040) and dysplastic (AHM2221) PDOs with nuclear fluorescent tags (H2B-GFP/mCherry) and imaged using time-lapse microscopy. Unlike the characteristic solid morphology of OAC PDOs[16], non-dysplastic PDOs showed four characteristic

543 morphologies: a single cell layer surrounding a single lumen, a single cell layer with multiple
544 lumens, multiple cell layers with a lumen and a solid morphology with no visible lumen **(Figure**
545 **3, A to C)**. Luminal PDOs expanded over time, whereas solid structures showed minimal growth
546 **(Supplementary Table 3).** In contrast, dysplastic PDOs lack single cell layer multiple lumen
547 morphology and have a higher proportion of solid morphology compared with non-dysplastic
548 PDOs **(Figure 3D, Supplementary Figure 5, A to C; Supplementary Table 4)**.
549
550 We observed minimal growth in almost all solid non-dysplastic organoids but visible expansion
551 in luminal types, measured by both organoid size and nuclear number **(Supplementary Figure 5,**
552 **D and E)**. Moreover, multiple and single lumen non-dysplastic PDOs demonstrated a similar,
553 linear growth rate with considerable variation in individual PDO growth **(Supplementary Figure**
554 **5, F and G)**. Growth kinetics of single-lumen PDOs were comparable between non-dysplastic and
555 dysplastic models **(Figure E, Supplementary Figure 5H)**. Time-lapse imaging also suggested
556 that multi-lumen PDOs might be a result of fusion events from single luminal PDOs, providing a
557 novel insight into the changing clonality of bulk organoid culture over time **(Supplementary**
558 **Figure 5, I and J).**
559
560 Lumen formation has been linked to polarity, the loss of which is associated with dysplastic
561 progression[46]. We established a lattice-based multi-site Cellular Potts Monte Carlo *in silico*
562 model of organoid growth in which organoid polarity, and the probability of a daughter organoid
563 exhibiting polarity, were varied **(Supplementary Figure 6A)**. Using this model, we demonstrate
564 that a single layer single lumen morphology is acquired where organoids and their progeny
565 demonstrate polarity, whereas organoids without polarity develop solid non-luminal structures
566 **(Supplementary Figure 6B)**. Variation in the probability of acquiring polarity results in a variability
567 in lumen formation **(Figure 3F)**. The model also accurately recreated the effects of observed
568 fusion processes **(Supplementary Figure 6, C to E)** and captured the loss of polarity in dysplastic
569 and OAC PDOs **(Supplementary Table 5).**
570
571 **Barrett oesophagus PDOs offer a functional platform for premalignant studies**
572 To extend the phenotypic characterisation we used transcriptomic profiling based on lineage
573 markers determined from our previous scRNA-seq datasets[5, 47]. As expected, the majority of BO
574 PDOs demonstrated an intermediate phenotype between that seen for gastric and intestinal
575 PDOs **(Figure 4A, Supplementary Figure 7, A and B)**. When comparing the bulk transcriptomes
576 of normal and precancerous PDOs using a principal component analysis (PCA), BO and intestinal

577 PDOs show a clear separation from gastric PDOs, in keeping with the acquisition of an intestinal
578 phenotype **(Figure 4B)**. When comparing differentially expressed genes (DEGs) between three
579 paired comparisons: gastric versus non-dysplastic PDOs, gastric versus dysplastic PDOs, and
580 non-dysplastic versus dysplastic PDOs, broad concordance was observed in non-dysplastic and
581 dysplastic PDOs when compared with gastric, while a small number of genes distinguished
582 dysplastic and non-dysplastic PDOs **(Figure 4, C and D, Supplementary Figure 7, C to E)**.
583 Pathway analyses revealed that upregulated genes in both non-dysplastic and dysplastic PDOs
584 were enriched for developmental, migratory, proliferative, and intestinal differentiation programs
585 **(Figure 4E, Supplementary Table 6)**, whereas down-regulated genes mapped to cell-peripheral
586 processes and transcription factor binding sites **(Figure 4E, Supplementary Table 6)**. In addition,
587 upregulation of extracellular matrix–related genes were specifically enriched in non-dysplastic
588 PDOs **(Supplementary Figure 7F, Supplementary Table 7),** while in dysplastic PDOs, down-
589 regulated genes mirrored the transcription factor binding site enrichment observed in the shared
590 down-regulated profiles **(Supplementary Figure 7G, Supplementary Table 8)**. Intriguingly, three
591 *HOX* genes (*HOXB2, HOXB6, HOXB8*), showed increased expression in dysplastic versus non-
592 dysplastic PDOs **(Figure 4, D and F)**, with a similar pattern also observed for *HOXB5* and *HOXB7*
593 **(Supplementary Figure 7H)**. This is consistent with our prior work demonstrating a role for HOX
594 genes in OAC carcinogenesis[48].
595
596 **Assembloid epithelial-fibroblast co-cultures recapitulate the role of fibroblasts in BO**
597 **development**
598 We have previously shown that BO acquires a pro-tumourigenic, activated fibroblast
599 environment, characterised by a reduction in the $CD34^+$ S1 fibroblast subset and an increase in
600 the αSMA^+ S3 subset[47]. However, the origin of this shift in fibroblast composition remains
601 unclear[19]. We reasoned that naïve fibroblasts could be reprogrammed into a BO-favoured niche
602 through a combination of intrinsic and extrinsic factors. To explore this, we built on a previously
603 described model to embed human primary oesophageal fibroblasts with BO or control normal
604 gastric PDOs **(Supplementary Figure 8A)**[49]. The resultant assembloids closely resembled
605 primary tissue, including with respect to glandular structures and stromal deposition
606 **(Supplementary Figure 8B)**.
607
608 We next sought to determine whether BO PDOs, either alone or in combination with pathological
609 microenvironmental stressors, could induce fibroblast reprogramming. To test this, we
610 characterised fibroblast subtypes in assembloids subjected to treatments mimicking reflux and

611 chronic local inflammation, which are the two key environmental factors associated with the
612 development and progression of BO. For experimental consistency, we used chemically defined
613 glycocholic acid, a bile acid component known to be highly effective in promoting BO
614 development[50]. In addition, we re-analysed our previous RNA-seq data to identify a relevant pro-
615 inflammatory exposure and selected interleukin 10 (IL10), a cytokine that shows a significant and
616 progressive increase during BO and OAC progression **(Supplementary Figure 9)**[51].
617
618 After treatment with reflux salt and/or IL10 for 7 days PDOs were dissociated into single cells and
619 analysed by flow cytometry **(Supplementary Figure 8C).** Reflux acid and IL10 treatment generally
620 reduced the proportion of S1 fibroblasts and increased the proportion of S3 fibroblasts
621 **(Supplementary Figure 8, D and E)**. However, this effect was much stronger in assembloids with
622 BO PDOs, which showed a markedly greater capacity to polarise fibroblasts towards the S3
623 subtype, particularly under reflux acid exposure. In contrast, normal gastric PDOs required both
624 reflux acid and IL10 to induce S3 fibroblasts, and the effect was comparatively modest.
625 **(Supplementary Figure 8F)**.
626
627 **OAC PDOs recapitulate population-level molecular heterogeneity with variable growth**
628 **behaviours**
629 The phenotypic and molecular heterogeneity that defines Barrett oesophagus is also a
630 characteristic feature of OAC[13]. Expanding on our previous small panel of 10 OAC PDOs[16], we
631 show here that a biobank of 38 PDOs (donor characteristics outlined in **Table 2**) recapitulates the
632 genomic landscape and known driver gene landscape for OAC[11, 52] **(Figure 5, A and B,**
633 **Supplementary Figures 10 and 11)**. Mirroring prior studies from patient samples[11, 52], alterations
634 in PDOs were enriched for copy-number alterations (22.2%) rather than point mutations or small
635 insertion-deletion mutations, even using stringent thresholds for amplifications and deletions.
636 As with patient series, *TP53* was the most frequently altered gene (70%) in the profiled PDOs,
637 followed by *CDKN2A* (22%), *ARID1A* (18%), *GATA6* (18%), and *SMAD4* (10%), although again
638 concordance with matching tissues varied and 16% (n=4/25) showed absence of a *TP53*
639 mutation, compared with *TP53*-mutant matching tissues **(Figure 5C and Supplementary Figure**
640 **11)**.
641
642 As in BO, there was broad alignment in the mutational signature landscape of PDOs and matching
643 tissues (median cosine similarity 0.98, range 0.74-1.00; **Figure 5D**). All previously reported[53] OAC
644 signatures (SBS17a/b, SBS18, SBS40, SBS1 and SBS5) were present **(Supplementary Figure 10I),**

645 with strong PDO–tissue concordance in the BO and OAC-defining[53, 54] SBS17a (r=0.92, p=4.1x10^{-}
646 ^{14}) and SBS17b (r=0.92, p=5.7x10^{-14}) signatures **(Supplementary Figure 10J)**. Compared with their
647 premalignant equivalents, OAC PDOs displayed increased SBS17a/b, SBS40, and marginal
648 increases in APOBEC-related SBS2/13 **(Supplementary Figure 10K)**. The OAC PDO
649 transcriptomic profile was variable, though there we did not observe specific gene expression
650 signatures that distinguished different groups of PDOs **(Figure 5E, Supplementary Figure 10, L**
651 **and M).** We also observed recurrent, ploidy-adjusted copy number gains (≥2 relative to sample
652 ploidy) in key oncogenes, including of the receptor tyrosine kinase HER2 in three PDOs, with
653 related protein overexpression **(Supplementary Figure 12).**
654
655 To compare OAC PDOs with BO growth metrics, we again used high-resolution time-lapse
656 microscopy **(Supplementary Figure 13, A to C)** Unlike BO, organoids with a solid structure
657 represented 99% of OAC PDOs observed at all assessed timepoints **(Supplementary Table 9)**.
658 Single cells contributing to OAC PDOs were significantly larger than those forming BO PDOs
659 **(Supplementary Figure 13D)** but demonstrated a similar growth rate **(Supplementary Figure**
660 **13E)**. A majority of PDOs grew in the seven days after seeding and did so with minimal underlying
661 variation in their growth rates **(Supplementary Figure 13, F and G)**, while some organoids more
662 rapidly increased in size because of fusion events **(Supplementary Figure 13H)**.
663
664 **OAC PDOs reproducibly show variable responses to anti-cancer therapies in keeping with**
665 **their molecular and phenotypic heterogeneity**
666 For OAC a key question is whether PDO phenotypic and molecular diversity translates to
667 differences between PDOs in their sensitivity to specific forms of systemic anti-cancer therapy
668 as well as external beam radiotherapy (EBRT), and whether the individual characteristics of each
669 PDO result in differences in sensitivity to individual chemotherapeutics, targeted agents and
670 EBRT. To assess this, five PDOs derived from treatment-naïve donors (OESO117, OESO146,
671 CAM277, CAM408, CAM574) were first exposed to the microtubule inhibitor (docetaxel), anti-
672 metabolite (5-fluorouracil (5-FU), with leucovorin) and platinum (oxaliplatin) constituents of the
673 current perioperative standard-of-care regimen, FLOT **(Figure 6A, Supplementary Table 10)**.
674 Mean IC_{50} values were lowest for docetaxel and demonstrated minimal variation between studied
675 PDOs (1.41–3.04 nM), whereas IC_{50} values for 5-FU/leucovorin (8.50–56.25 μM) and oxaliplatin
676 (IC_{50} 9.24–93.57 μM) were higher and demonstrate substantial variation. In contrast,
677 5FU/leucovorin E_{max} values were 94% or above in all but one PDO but varied between 69.7-96.2%
678 for oxaliplatin, and between 48.7-93.5% for docetaxel. Validating the utility of using PDOs as a

679 pharmacokinetic model, there was no correlation between IC_{50} and E_{max} values for 5-
680 FU/leucovorin (r=0.10, p=0.87), oxaliplatin (r=-0.58, p=0.31) or docetaxel (r=0.33, p=0.58). We
681 also demonstrated a heterogeneity of response to external beam x-ray irradiation **(Figure 6B,**
682 **Supplementary Table 11)**. Organoid forming efficiency varied between 0.42-1.03 in response to
683 a standard 2Gy single fraction of EBRT, and between 0.24-0.75 in response to a high 8Gy single
684 fraction. This corresponded to an integral area under the curve (AUC) for response to 0-8Gy
685 single-fraction irradiation of between 0.46-0.98.
686
687 We and others have also previously reported that as many as 50% of cases of OAC contain
688 sensitising events for CDK inhibitors[11]. However, the extent to which this translates to a
689 consistent therapeutic response across an otherwise heterogenous population is uncertain.
690 Using four PDOs with relevant vulnerabilities (CAM277, CAM401, CAM429, CAM535), we
691 demonstrate diverse sensitivity to the CDK4/6 inhibitor abemaciclib (IC_{50} 0.59–2.87 μM, Emax 36–
692 70%) **(Figure 6C, Supplementary Table 12)**. Activity was greatest in CAM277 (KRAS ecDNA, IC_{50}
693 0.91 μM, Emax 70%), intermediate in CDK6-amplified PDOs CAM429 (0.59 μM, 49%) and CAM535
694 (1.30 μM, 49%), and weakest in CAM401 (KRAS nuclear amplified; 2.87 μM, 36%) exemplifying the
695 importance of being able to match the PDO specific genomic profile with the therapy response.
696
697 As outlined in **Figure 6D**, individual PDO sensitivity to different forms of cytotoxic chemotherapy
698 and to EBRT varied. Overall, chemotherapy sensitivity did not predict radiotherapy sensitivity.
699 However, differences in relative sensitivity to oxaliplatin were similar to differences in relative
700 sensitivity to EBRT.
701
702 **DISCUSSION**
703 Inter- and intra- lesional heterogeneity are fundamental, hard-to-study barriers to the effective
704 prevention and treatment of OAC[13]. Here, we derive and comprehensively characterise a biobank
705 of 116 PDOs and sc-organoids that recapitulate disease heterogeneity in BO and OAC, including
706 within lesions as well as across patient populations. As summarised in **Table 3,** we demonstrate
707 that the specific position each PDO has in the malignant spectrum cannot be discerned from a
708 single feature and nor can it be assumed from the characteristics of the matching tissue due to
709 the extreme heterogeneity. Instead, the functionally relevant disease state of a given PDO can be
710 deduced from a multi-level assessment of genomic, transcriptomic, protein and morphological
711 characteristics **(Supplementary Figure 14)**. In this manuscript we also provide tools for
712 supporting the quantitative characterisation of PDOs at the molecular and phenotypic level, and

713 demonstrate that sc-organoids help capture subclonal heterogeneity and allow for the
714 maintenance of high-risk populations that are otherwise lost over serial passages. Further, we
715 show that individuals PDOs demonstrate variable sensitivity to EBRT and different forms of
716 systemic anti-cancer therapy, and that responses to these treatments vary across the PDO
717 population. In so doing, we demonstrate the utility of PDOs for studying high-risk disease features
718 in the context of premalignant disease, as well as for analysing variable treatment responses in
719 cancer.
720
721 Previous attempts to model BO neoplastic progression have relied on animal models and
722 xenografts that poorly recapitulate the anatomical and biological features of human disease[55].
723 PDOs are in theory more scalable and have been used to study carcinogenesis in other contexts,
724 such as for colorectal cancer[56, 57]. However, there is a long recognised challenge to establishing
725 and propagating BO PDO cultures, with reported success rates for establishing BO PDOs of
726 between 0-70%[55]. Here, we demonstrate derivation of 21 PDOs from regions of non-dysplastic
727 and dysplastic BO with success rates of 68% and 61%, respectively. All remained viable over
728 multiple passages, and all were successfully recovered from cryopreservation. This contrasts
729 with our previous unsuccessful attempts to derive BO PDOs[16], which likely reflects the addition
730 to culture medium of gastrin and FGF10[55].
731
732 There is also uncertainty as to the degree to which PDOs can be used to study BO dysplastic
733 progression. Previous attempts to develop a model for OAC carcinogenesis have primarily
734 focussed on gene editing of BO or normal gastroesophageal junctional PDOs[58, 59]. However,
735 genetic manipulation in this context is inefficient and poor survival rates result in selection and
736 propagation of monoclonal populations[58, 59]. Our work and that of others has also shown that OAC
737 very likely always derives from BO[5, 60, 61], which questions the relevance of modelling dysplastic
738 progression using normal gastroesophageal junctional PDOs. To this end, studies in colorectal
739 cancer have demonstrated that modelling tumourigenesis using normal tissue PDOs as a starting
740 point fails to capture many of the known molecular changes that accompany the development of
741 invasive disease[56, 57]. There is therefore a need to model progression using PDOs derived from
742 premalignant tissue.
743
744 Our comprehensive genomic, transcriptomic and phenotypic characterisation of BO PDO
745 cultures demonstrates that whilst PDOs derived from dysplastic tissue exhibited more cancer-
746 like genomic alterations than those derived from non-dysplastic tissue, they have lower

747 concordance with matching tissue. Concordance with matching tissue was also generally lower
748 for BO than it was for OAC PDOs. This is likely to be due to the nature of heterogeneity in BO, which
749 is characterised by the presence of distinct clones that do not sweep the entire segment and
750 instead arise through clonal expansion that occurs on a scale of millimetres[7, 62].
751
752 We reasoned that it is also possible that high risk subclonal populations may not be adequately
753 reflected in bulk PDO sequencing and may be lost over time or through passaging. To counter
754 this, we demonstrate a technique to isolate sc-organoids, which we show can isolate high risk
755 subclones that may not be represented in bulk PDO sequencing. These can then serve as
756 observable functional proxies for intralesional heterogeneity at a single clone level, with each
757 demonstrating varying degrees of malignant potential. Integrating these clones into the
758 epithelial–fibroblast assembloid system we describe here would enable testing of whether
759 specific high-risk lineages differentially polarise fibroblasts under pathological cues that, in turn,
760 promote their expansion and drive disease progression. Looking ahead, incorporating immune
761 cells, such as autologous or allogeneic tissue-resident myeloid or T-cell populations, and
762 immunogenic cytokines into this platform would allow interrogation of how epithelial and stromal
763 evolution interfaces with emerging immune microenvironments during early cancer development
764 and progression.
765
766 As well as being able to recapitulate the substantial heterogeneity in OAC organoids, we also
767 show that we can recapitulate the diverse treatment responses seen in patients with OAC,
768 demonstrating highly variable responses to each of the individual components of the standard
769 preoperative regimen, FLOT[14]. There is, for example, consistently high sensitivity (i.e. low IC_{50}
770 values) to docetaxel, though this has a variable maximum effect (i.e. E_{max}). In contrast, PDOs have
771 a lower and more variable sensitivity to 5-FU/leucovorin, though this consistently exerts a high
772 maximal effect when added to PDOs at a sufficiently high concentration. This mirrors clinical
773 data, where 5FU/leucovorin is the backbone of most chemotherapy regimens in OAC due to a
774 conserved effect across the entire patient population[63]. It is similarly interesting that
775 chemotherapy sensitivity does not mirror radiation or CDK inhibitor sensitivity, which provides
776 biological rationale for an expanding portfolio of studies that are combining intensified
777 preoperative chemotherapy with chemoradiotherapy or targeted agents. It would be of interest to
778 determine whether the application of the PDOs described here to an organ-on-chip approach,
779 such as that described by *Pal et al*[17], would further improve modelling of therapeutic response.
780

In summary, we have developed a comprehensively characterised biobank of BO and OAC PDOs that reflect known disease heterogeneity across pre-malignant and invasive disease. Careful characterisation is essential to understand the providence of a given organoid and derivation of sc-organoids allows for the analysis of high-risk clones. Together, these models provide a scalable platform for functional studies of OAC carcinogenesis and therapeutic response.

ACKNOWLEDGEMENTS

This work was directly supported by grants from Cancer Research UK (CRUK) to L.Z. (A31116 and EDDPJT-May23/100046) and C.M.J. (RNPSF-Jan23/100006), from the Academy of Medical Sciences to C.M.J. (SGL030\1032), and by a Medical Research Council Programme Grant awarded to R.C.F. (MR/W014122/1). The Oesophageal Cancer Clinical & Molecular Stratification (OCCAMS) study and its successor OCCAMS 2 study were funded by Programme Grant funding (A15874, A22720, A22131) from CRUK. D.P.M. is supported by a Clinical Research Training Fellowship supported by the CRUK Cambridge Centre (SEBCATP-2024/100008). C.M.J. is supported by a Clinical Lectureship partly funded by CRUK RadNet Cambridge (C17918/A28870). The authors are grateful to the Human Research Tissue Bank at Addenbrooke's Hospital, Cambridge University Hospitals NHS Foundation Trust, and for the support provided to it by the National Institute for Health Research (NIHR) Cambridge Biomedical Research Centre (BRC-1215-200014). The views expressed are those of the authors and not necessarily those of the NIHR or the Department of Health and Social Care. The authors are grateful for the materials provided by the Jacqueline Shields Group, King's College London, and the Fiona Gribble Group, University of Cambridge.

AUTHOR CONTRIBUTIONS

R.C.F., C.M.J. and L.Z. conceived the manuscript, obtained funding and oversaw the work. C.M.J. conceived therapeutic analyses in OAC PDOs. L.Z. conceived studies relating to Barrett oesophagus PDOs, single cell-derived clonal organoid and assembloid. D.H.J., G.D. and SG.J. conducted bioinformatic and computational analyses. D.P.M., C.C., T.S.C., H.C., X.L., A.M., C.M.J. and L.Z. performed wet laboratory experiments and led or contributed to experimental design. E.B. and B.H. conducted the in-silico analysis of organoid morphologies. K.T.M., M.dP. and K.S-P. contributed to sample collection, curation and characterisation. D.H.J., D.P.M., R.C.F., C.M.J. and L.Z. wrote the first draft of the manuscript. All authors contributed to subsequent revisions and all have read and approved the manuscript.

DECLARATION OF INTERESTS

C.M.J. has received consultancy fees from Candesic for work outside the scope of this manuscript. R.C.F. is a co-founder and shareholder in Cyted Health, sits on the advisory board for AstraZeneca and CRUK Functional Genomics Centre, and consults for AstraZeneca and 23andMe.

References

1. Morgan E, Soerjomataram I, Gavin AT, Rutherford MJ, Gatenby P, Bardot A, et al. International trends in oesophageal cancer survival by histological subtype between 1995 and 2014. Gut. 2021;70(2):234-42.
2. Morgan E, Soerjomataram I, Rumgay H, Coleman HG, Thrift AP, Vignat J, et al. The Global Landscape of Esophageal Squamous Cell Carcinoma and Esophageal Adenocarcinoma Incidence and Mortality in 2020 and Projections to 2040: New Estimates From GLOBOCAN 2020. Gastroenterology. 2022;163(3):649-58.e2.
3. Thrift AP. Global burden and epidemiology of Barrett oesophagus and oesophageal cancer. Nat Rev Gastroenterol Hepatol. 2021;18(6):432-43.
4. Souza RF, Spechler SJ. Mechanisms and pathophysiology of Barrett oesophagus. Nat Rev Gastroenterol Hepatol. 2022;19(9):605-20.
5. Nowicki-Osuch K, Zhuang L, Jammula S, Bleaney CW, Mahbubani KT, Devonshire G, et al. Molecular phenotyping reveals the identity of Barrett's esophagus and its malignant transition. Science. 2021;373(6556):760-7.
6. Hvid-Jensen F, Pedersen L, Drewes AM, Sørensen HT, Funch-Jensen P. Incidence of adenocarcinoma among patients with Barrett's esophagus. N Engl J Med. 2011;365(15):1375-83.
7. Ross-Innes CS, Becq J, Warren A, Cheetham RK, Northen H, O'Donovan M, et al. Whole-genome sequencing provides new insights into the clonal architecture of Barrett's esophagus and esophageal adenocarcinoma. Nat Genet. 2015;47(9):1038-46.
8. Maley CC, Galipeau PC, Finley JC, Wongsurawat VJ, Li X, Sanchez CA, et al. Genetic clonal diversity predicts progression to esophageal adenocarcinoma. Nat Genet. 2006;38(4):468-73.
9. Martinez P, Timmer MR, Lau CT, Calpe S, Sancho-Serra Mdel C, Straub D, et al. Dynamic clonal equilibrium and predetermined cancer risk in Barrett's oesophagus. Nat Commun. 2016;7:12158.
10. Deboever N, Jones CM, Yamashita K, Ajani JA, Hofstetter WL. Advances in diagnosis and management of cancer of the esophagus. BMJ. 2024;385:e074962.
11. Frankell AM, Jammula S, Li X, Contino G, Killcoyne S, Abbas S, et al. The landscape of selection in 551 esophageal adenocarcinomas defines genomic biomarkers for the clinic. Nat Genet. 2019;51(3):506-16.
12. Noorani A, Li X, Goddard M, Crawte J, Alexandrov LB, Secrier M, et al. Genomic evidence supports a clonal diaspora model for metastases of esophageal adenocarcinoma. Nat Genet. 2020;52(1):74-83.
13. McClurg DP, Pan S, Fitzgerald RC, Jones CM. The biology and therapeutic implications of heterogeneity in Barrett oesophagus and oesophageal adenocarcinoma. Nat Rev Clin Oncol. 2025.

14. Hoeppner J, Brunner T, Schmoor C, Bronsert P, Kulemann B, Claus R, et al. Perioperative Chemotherapy or Preoperative Chemoradiotherapy in Esophageal Cancer. N Engl J Med. 2025;392(4):323-35.
15. Kapoor H, Lohani KR, Lee TH, Agrawal DK, Mittal SK. Animal Models of Barrett's Esophagus and Esophageal Adenocarcinoma-Past, Present, and Future. Clin Transl Sci. 2015;8(6):841-7.
16. Li X, Francies HE, Secrier M, Perner J, Miremadi A, Galeano-Dalmau N, et al. Organoid cultures recapitulate esophageal adenocarcinoma heterogeneity providing a model for clonality studies and precision therapeutics. Nat Commun. 2018;9(1):2983.
17. Pal S, Shimshoni E, Torres SF, Kong M, Tai K, Sangwan V, et al. Patient-derived esophageal adenocarcinoma organ chip: a physiologically relevant platform for functional precision oncology. J Transl Med. 2025;23(1):577.
18. Ooft SN, Weeber F, Dijkstra KK, McLean CM, Kaing S, van Werkhoven E, et al. Patient-derived organoids can predict response to chemotherapy in metastatic colorectal cancer patients. Sci Transl Med. 2019;11(513).
19. Strasser MK, Gibbs DL, Gascard P, Bons J, Hickey JW, Pan D, et al. Concerted changes in Epithelium and Stroma: a multi-scale, multi-omics analysis of progression from Barrett's Esophagus to adenocarcinoma. Dev Cell. 2025.
20. Walker RC, Breininger SP, Sharpe BP, Harrington J, Reddin I, Tse C, et al. Cancer-associated fibroblasts are associated with neo-adjuvant treatment response in oesophageal adenocarcinoma. Br J Cancer. 2025;133(5):633-47.
21. Cheung TS, Giacomini C, Cereda M, Avivar-Valderas A, Capece D, Bertolino GM, et al. Apoptosis in mesenchymal stromal cells activates an immunosuppressive secretome predicting clinical response in Crohn's disease. Mol Ther. 2023;31(12):3531-44.
22. Schmäche T, Fohgrub J, Klimova A, Laaber K, Drukewitz S, Merboth F, et al. Stratifying esophago-gastric cancer treatment using a patient-derived organoid-based threshold. Mol Cancer. 2024;23(1):10.
23. Kosovec JE, Zaidi AH, Omstead AN, Matsui D, Biedka MJ, Cox EJ, et al. CDK4/6 dual inhibitor abemaciclib demonstrates compelling preclinical activity against esophageal adenocarcinoma: a novel therapeutic option for a deadly disease. Oncotarget. 2017;8(59):100421-32.
24. Francies HE, Barthorpe A, McLaren-Douglas A, Barendt WJ, Garnett MJ. Drug Sensitivity Assays of Human Cancer Organoid Cultures. Methods Mol Biol. 2019;1576:339-51.
25. Li H, Durbin R. Fast and accurate short read alignment with Burrows-Wheeler transform. Bioinformatics. 2009;25(14):1754-60.
26. Saunders CT, Wong WS, Swamy S, Becq J, Murray LJ, Cheetham RK. Strelka: accurate somatic small-variant calling from sequenced tumor-normal sample pairs. Bioinformatics. 2012;28(14):1811-7.
27. Ng AWT, Contino G, Killcoyne S, Devonshire G, Hsu R, Abbas S, et al. Rearrangement processes and structural variations show evidence of selection in oesophageal adenocarcinomas. Commun Biol. 2022;5(1):335.
28. Telli ML, Timms KM, Reid J, Hennessy B, Mills GB, Jensen KC, et al. Homologous Recombination Deficiency (HRD) Score Predicts Response to Platinum-Containing Neoadjuvant Chemotherapy in Patients with Triple-Negative Breast Cancer. Clin Cancer Res. 2016;22(15):3764-73.

29. Sztupinszki Z, Diossy M, Krzystanek M, Reiniger L, Csabai I, Favero F, et al. Migrating the SNP array-based homologous recombination deficiency measures to next generation sequencing data of breast cancer. NPJ Breast Cancer. 2018;4:16.
30. Islam SMA, Díaz-Gay M, Wu Y, Barnes M, Vangara R, Bergstrom EN, et al. Uncovering novel mutational signatures by de novo extraction with SigProfilerExtractor. Cell Genom. 2022;2(11):None.
31. Rosenthal R, McGranahan N, Herrero J, Taylor BS, Swanton C. DeconstructSigs: delineating mutational processes in single tumors distinguishes DNA repair deficiencies and patterns of carcinoma evolution. Genome Biol. 2016;17:31.
32. Gillis S, Roth A. PyClone-VI: scalable inference of clonal population structures using whole genome data. BMC Bioinformatics. 2020;21(1):571.
33. Schliep KP. phangorn: phylogenetic analysis in R. Bioinformatics. 2011;27(4):592-3.
34. Love MI, Huber W, Anders S. Moderated estimation of fold change and dispersion for RNA-seq data with DESeq2. Genome Biol. 2014;15(12):550.
35. Kolberg L, Raudvere U, Kuzmin I, Vilo J, Peterson H. gprofiler2 -- an R package for gene list functional enrichment analysis and namespace conversion toolset g:Profiler. F1000Res. 2020;9.
36. Hänzelmann S, Castelo R, Guinney J. GSVA: gene set variation analysis for microarray and RNA-seq data. BMC Bioinformatics. 2013;14:7.
37. Leek JT, Johnson WE, Parker HS, Jaffe AE, Storey JD. The sva package for removing batch effects and other unwanted variation in high-throughput experiments. Bioinformatics. 2012;28(6):882-3.
38. Kita-Matsuo H, Barcova M, Prigozhina N, Salomonis N, Wei K, Jacot JG, et al. Lentiviral vectors and protocols for creation of stable hESC lines for fluorescent tracking and drug resistance selection of cardiomyocytes. PLoS One. 2009;4(4):e5046.
39. Ng AWT, McClurg DP, Wesley B, Zamani SA, Black E, Miremadi A, et al. Disentangling oncogenic amplicons in esophageal adenocarcinoma. Nat Commun. 2024;15(1):4074.
40. Schindelin J, Arganda-Carreras I, Frise E, Kaynig V, Longair M, Pietzsch T, et al. Fiji: an open-source platform for biological-image analysis. Nat Methods. 2012;9(7):676-82.
41. Schindelin J, Rueden CT, Hiner MC, Eliceiri KW. The ImageJ ecosystem: An open platform for biomedical image analysis. Mol Reprod Dev. 2015;82(7-8):518-29.
42. Swat MH, Thomas GL, Belmonte JM, Shirinifard A, Hmeljak D, Glazier JA. Multi-scale modeling of tissues using CompuCell3D. Methods Cell Biol. 2012;110:325-66.
43. Barrett MT, Sanchez CA, Galipeau PC, Neshat K, Emond M, Reid BJ. Allelic loss of 9p21 and mutation of the CDKN2/p16 gene develop as early lesions during neoplastic progression in Barrett's esophagus. Oncogene. 1996;13(9):1867-73.
44. Luebeck J, Ng AWT, Galipeau PC, Li X, Sanchez CA, Katz-Summercorn AC, et al. Extrachromosomal DNA in the cancerous transformation of Barrett's oesophagus. Nature. 2023.
45. . !!! INVALID CITATION !!! 44, 45.
46. Peters Y, Al-Kaabi A, Shaheen NJ, Chak A, Blum A, Souza RF, et al. Barrett oesophagus. Nat Rev Dis Primers. 2019;5(1):35.
47. Nowicki-Osuch K, Zhuang L, Cheung TS, Black EL, Masque-Soler N, Devonshire G, et al. Single-cell RNA sequencing unifies developmental programs of Esophageal and Gastric Intestinal Metaplasia. Cancer Discov. 2023.

48. di Pietro M, Lao-Sirieix P, Boyle S, Cassidy A, Castillo D, Saadi A, et al. Evidence for a functional role of epigenetically regulated midcluster HOXB genes in the development of Barrett esophagus. Proc Natl Acad Sci U S A. 2012;109(23):9077-82.
49. Seino T, Kawasaki S, Shimokawa M, Tamagawa H, Toshimitsu K, Fujii M, et al. Human Pancreatic Tumor Organoids Reveal Loss of Stem Cell Niche Factor Dependence during Disease Progression. Cell Stem Cell. 2018;22(3):454-67.e6.
50. Straub D, Oude Elferink RPJ, Jansen PLM, Bergman J, Parikh K, Krishnadath KK. Glyco-conjugated bile acids drive the initial metaplastic gland formation from multi-layered glands through crypt-fission in a murine model. PLoS One. 2019;14(7):e0220050.
51. Jammula S, Katz-Summercorn AC, Li X, Linossi C, Smyth E, Killcoyne S, et al. Identification of Subtypes of Barrett's Esophagus and Esophageal Adenocarcinoma Based on DNA Methylation Profiles and Integration of Transcriptome and Genome Data. Gastroenterology. 2020;158(6):1682-97.e1.
52. Weaver JMJ, Ross-Innes CS, Shannon N, Lynch AG, Forshew T, Barbera M, et al. Ordering of mutations in preinvasive disease stages of esophageal carcinogenesis. Nat Genet. 2014;46(8):837-43.
53. Abbas S, Pich O, Devonshire G, Zamani SA, Katz-Summercorn A, Killcoyne S, et al. Mutational signature dynamics shaping the evolution of oesophageal adenocarcinoma. Nat Commun. 2023;14(1):4239.
54. Secrier M, Li X, de Silva N, Eldridge MD, Contino G, Bornschein J, et al. Mutational signatures in esophageal adenocarcinoma define etiologically distinct subgroups with therapeutic relevance. Nat Genet. 2016;48(10):1131-41.
55. Milne JV, Mustafa EH, Clemons NJ. Modelling esophageal adenocarcinoma and Barrett's esophagus with patient-derived organoids. Front Mol Biosci. 2024;11:1382070.
56. Drost J, van Jaarsveld RH, Ponsioen B, Zimberlin C, van Boxtel R, Buijs A, et al. Sequential cancer mutations in cultured human intestinal stem cells. Nature. 2015;521(7550):43-7.
57. Matano M, Date S, Shimokawa M, Takano A, Fujii M, Ohta Y, et al. Modeling colorectal cancer using CRISPR-Cas9-mediated engineering of human intestinal organoids. Nat Med. 2015;21(3):256-62.
58. Liu X, Cheng Y, Abraham JM, Wang Z, Wang Z, Ke X, et al. Modeling Wnt signaling by CRISPR-Cas9 genome editing recapitulates neoplasia in human Barrett epithelial organoids. Cancer Lett. 2018;436:109-18.
59. Zhao H, Cheng Y, Kalra A, Ma K, Zheng Y, Ziman B, et al. Generation and multiomic profiling of a TP53/CDKN2A double-knockout gastroesophageal junction organoid model. Sci Transl Med. 2022;14(673):eabq6146.
60. Curtius K, Rubenstein JH, Chak A, Inadomi JM. Computational modelling suggests that Barrett's oesophagus may be the precursor of all oesophageal adenocarcinomas. Gut. 2020;70(8):1435-40.
61. Zamani SAW, L; Black E. L.; Bartram, A.; Ng A. W. T.; Secrier, M.; Perelman, J. D.; Ustaoglu, A.; Ococks E. L.; Jacobson, D.; Devonshire, G.; Grehan, N.; Nutzinger, B.; Freeman, A.; Miremadi, A.; O'Donovan, M.; Frankell, A. M.; Killcoyne, S.; OCCAMS Consortium; Coleman, H. G.; Fitzgerald, R. C. Integrated epidemiological and molecular data yields insights into the relationship between precancer and cancer states of oesophageal adenocarcinoma Nature Medicine. 2026.

62. Martinez P, Mallo D, Paulson TG, Li X, Sanchez CA, Reid BJ, et al. Evolution of Barrett's esophagus through space and time at single-crypt and whole-biopsy levels. Nat Commun. 2018;9(1):794.
63. Al-Batran SE, Homann N, Pauligk C, Goetze TO, Meiler J, Kasper S, et al. Perioperative chemotherapy with fluorouracil plus leucovorin, oxaliplatin, and docetaxel versus fluorouracil or capecitabine plus cisplatin and epirubicin for locally advanced, resectable gastric or gastro-oesophageal junction adenocarcinoma (FLOT4): a randomised, phase 2/3 trial. Lancet. 2019;393(10184):1948-57.

1007 **LIST OF FIGURES**

1008 **Figure 1: The genomic landscape of normal gastric and Barrett oesophagus-derived PDOs**
1009 **and its correlation with parent tissue samples. (A)** Driver alterations and genomic features
1010 across PDOs and adjacent tissues. Driver genes were considered according to the set of genes
1011 (n=76) found to be positively selected in OAC by Frankell et al[11] **(B)** Concordance of mutational
1012 profiles across Barrett oesophagus tissue-PDO pairs, defined by the proportion of mutations
1013 shared and unique across samples. Tissues from normal stomach did not undergo WGS. **(C-D)**
1014 Comparisons of **(C)** indel and SNV burdens, and **(D)** ploidy across tissue-PDO pairs. **(E)**
1015 Comparisons of mutational signature profiles across tissue-PDO pairs calculated by cosine
1016 similarity. **(F)** Correlations in SBS17a (left) and SBS17b (right) proportions across tissue-PDO
1017 pairs. Pearson correlation coefficients were used to determine correlation strengths.

1018

1019 **Figure 2: Diversification of non-dysplastic Barrett oesophagus demonstrated in a single cell-**
1020 **derived clonal organoid panel. (A)** Approach for establishing sc-organoids. **(B)** Distributions of
1021 VAFs from single cell-derived organoids (n=19) derived from AHM2149. **(C)** Driver alterations
1022 found across the single cell-derived clonal organoid panel and adjacent bulk PDO and tissue. **(D)**
1023 A phylogenetic profile of organoids derived from AHM2149 defined using the sc-organoid panel.
1024 Signature contributions were calculated across mutations contributing to each branch
1025 respectively. Branch lengths are generally proportional to total amount of mutations. Signatures
1026 were not fitted for branches with fewer than 25 SNVs. **(E)** Hierarchical clustering of RNA-seq
1027 profiling for the sc-organoid panel using the top 500 variable genes following variance stabilised
1028 transformation of read counts. Heatmap annotation includes genetic alterations as reported in
1029 **(C)** and log2-transformed TPM-normalised counts of *MUC6* (a gastric marker) and *CDX2* (an
1030 intestinal markers), the correlation of which is reported in Supplementary Figure 6E. The coloured
1031 dashed squares found in **(D)** and **(E)** correspond to adjacent clones found through phylogenetic
1032 analysis and unsupervised clustering of RNA-seq.

1033

1034 **Figure 3: Analysis of key morphological features observed in Barrett oesophagus PDOs. (A)**
1035 Representative bright-field images showing the four morphology classes: a single cell layer
1036 surrounding a single lumen, a single cell layer with multiple lumens, multiple cell layers with a
1037 lumen and a solid morphology with no visible lumen. In all instances the red scale bar represents
1038 a length of 100μm. **(B)** Example field of view illustrating the coexistence of multiple morphologies
1039 within a single dome of non-dysplastic (AHM0040) Barrett oesophagus PDOs. Scale bar
1040 represents 200μm. **(C)** Stacked bar plot of the count of each morphology class over seven days

of growth following seeding in non-dysplastic (AHM0040) PDOs. **(D)** Proportional composition of morphologies at the indicated time points (normalised to total organoids measured per day) for dysplastic (AHM2221) PDOs. **(E)** Diameter squared (proportional to number of cells) of non-dysplastic (AHM0040) and dysplastic (AHM2221) PDOs at days 4 and 6 following seeding. **(F)** *In silico* simulations of organoid growth/morphology across four random seeds under three scenarios depicting variable likelihood of inheriting polarity (IP).

Figure 3: Transcriptomic profiling of control normal gastric and intestinal, and Barrett oesophagus, PDOs. (A) Inter-PDO expression of gastric- and intestinal-related genes. The reported scores were calculated using Z-normalisation following log2-transformation of TPM values. **(B)** Principal component analysis of all normal- and Barrett oesophagus PDOs based on the top 500 variable genes following variance stabilising transformation. **(C)** Correlations of log2-fold changes from differential expression analysis on non-dysplastic Barrett versus normal gastric, and dysplastic Barrett versus normal gastric PDOs. Genes were considered significant if they had an adjusted p-value < 0.05 and absolute log2-fold change > 1, as indicated by the dashed red lines. Full results of these analyses are reported in **Supplementary Figure 5D-E**. **(D)** Differential expression across dysplastic (n=5) versus non-dysplastic (n=9) Barrett oesophagus PDOs. Positive log2-fold change refers to increased expression in the dysplastic PDOs. Genes were coloured based on their adjusted p-value being less than 0.05, and absolute log2-fold change greater than 1. **(E)** Functional enrichment analysis of up- and down-regulated genes shared across non-dysplastic and dysplastic PDOs compared with normal gastric PDOs. Full functional enrichment analysis results are reported in **Supplementary Table 6**. **(F)** Expression of *HOXB2*, *HOXB6*, and *HOXB8* across all control normal and Barrett oesophagus PDOs. Values reported are log2-transformed TPM values, and comparison was done on the non-dysplastic and dysplastic PDOs using a two-sided Wilcoxon test with Benjamini-Hochberg adjustment for multiple testing.

Figure 5: An OAC PDO biobank captures parent tissue features and recapitulates multi-level population diversity. (A) Driver alterations and genomic features across OAC-derived PDOs and adjacent tissues. Driver genes were considered according to those previously defined by Frankell et al[11]. **(B)** Concordance of mutational profiles across OAC tissue-PDO pairs, defined by the proportion of mutations that are shared or unique across samples. **(C)** Circos plots demonstrating genomic features of OAC PDOs and their parent tissues. **(D)** Comparisons of mutational signature profiles across tissue-PDO pairs calculated by cosine similarity. **(E)**

1075 Principal component analysis of bulk RNAseq profiles of derived OAC PDOs and relationship to
1076 tumour stage.
1077
1078 **Figure 6: OAC PDOs demonstrate variable responses to chemotherapy, radiotherapy and**
1079 **targeted agents. (A)** Inhibitory concentration curves demonstrating the viability of five OAC PDOs
1080 following exposure to **(i)** docetaxel, **(ii)** 5-fluorouracil (5-FU) and leucovorin, or **(iii)** oxaliplatin. **(B)**
1081 Organoid forming efficiency following exposure to a single fraction of 0-8Gy x-ray irradiation for
1082 eight OAC PDOs. **(C)** Correlation between AUC organoid forming efficiency following x-ray
1083 irradiation and AUC viability values following exposure to 5-FU and leucovorin, oxaliplatin or
1084 docetaxel. **(D)** Inhibitory concentration curves demonstrating he viability of four OAC PDOs
1085 following exposure to the CDK4/6 inhibitor, abemaciclib. **(E)** Normalised AUC sensitivity values
1086 for each anti-cancer treatment across three separated PDOs (created in https://BioRender.com).

1087 **LIST OF SUPPLEMENTARY FIGURES**

1088 **Supplementary Figure 1: Schematic overview of the 116 normal, Barrett oesophagus and**
1089 **OAC bulk PDOs and single cell-derived organoids generated for this study.** The site from
1090 which samples were obtained, and the sampling route, is shown, as is a summary of the multi-
1091 level characterisation employed for all obtained models. Image generated using BioRender®.

1092

1093 **Supplementary Figure 2: Concordance of genomic features between Barrett oesophagus**
1094 **PDOs and their parent tissues.** Tumour mutation burden across **(A)** PDOs derived from normal
1095 gastric and BO tissue, and **(B**) tissues derived from non-dysplastic and dysplastic BO. **(C)**
1096 Differences in VAFs of shared mutations across PDO-tissue pairs, with the dotted red-line
1097 indicating mutations where $VAF_{organoid} - VAF_{tissue} = 0$ (i.e. where a mutation has equal VAF in a PDO
1098 and its adjacent tissue). **(D) (i)** Comparisons of tumour purity between adjacent tissues and
1099 PDOs, and **(ii)** comparisons of tumour purity between non-dysplastic and dysplastic Barrett
1100 oesophagus. Purity within PDO-tissue pairs was calculated via a pairwise Wilcoxon test, and
1101 purity across Barrett dysplastic stages was compared via a two-sample Wilcoxon test. **(E)**
1102 Comparisons of indel and SNV burdens across PDO-tissue pairs. Correlation strengths were
1103 reported as Pearson correlation coefficients. The black dotted line represents the line where (i.e.
1104 where the number of mutations is equal between a PDO and its adjacent tissue). **(F)**
1105 Comparisons of HRD index scores across PDO-tissue pairs, with Pearson correlation coefficients
1106 reported for non-dysplastic dysplastic BO derived samples. The black dotted line represents the
1107 line where $HRD_{organoid} = HRD_{tissue}$ (i.e. where the HRD index scores for a PDO is equal to
1108 that of its adjacent tissue). **(G)** Comparisons of cosine similarity scores of signature profiles as
1109 reported in **Figure 1F** and **Supplementary Figure 1D** across non-dysplastic and dysplastic
1110 Barrett oesophagus-derived PDO-tissue pairs. Similarity scores were compared using a two-
1111 sample Wilcoxon test. **(H)** Summary of mutational signature analysis on adjacent Barrett
1112 oesophagus-derived PDOs and tissues. Samples (rows) are ordered into PDO-tissue pairs. **(I)**
1113 Correlations in SBS17a/b contributions across PDO-tissue pairs with Pearson correlation
1114 coefficients calculated separately across non-dysplastic and dysplastic samples. **(J)**
1115 Comparisons of SBS17a/b contributions across non-dysplastic and dysplastic Barrett
1116 oesophagus-derived PDOs. Contributions were compared using two-sample Wilcoxon tests.
1117 Correction for multiple testing was conducted using the Benjamini-Hochberg procedure. **(K)** VAF
1118 distributions of AHM0040, a PDO derived from a non-dysplastic Barrett oesophagus case. Dotted
1119 lines represent the VAFs of mutations in OAC-associated driver genes. **(L)** VAF distributions of

1120 shared mutations at passages 1 and 6 of AHM1373, a non-dysplastic derived PDO. Colours refer
1121 to the clonal classifications of mutations at passage 1.
1122
1123 **Supplementary Figure 3: Clonal expansions of Barrett PDOs across passages and within a**
1124 **non-dysplastic Barrett-derived panel of single cell-derived clonal organoids. (A)** Tumour
1125 mutation burdens of the single cell-derived clonal organoid panel derived from a non-dysplastic
1126 Barrett oesophagus PDO (AHM2149), with mutations classified as those shared with the bulk
1127 organoid from which they were derived, those not captured in the bulk organoid but present in at
1128 least one derived organoid, and private mutations. **(B)** Signature contributions across all
1129 mutations from the single cell-derived clonal organoid panel and its adjacent tissue and bulk
1130 organoid. **(C)** Correlation between *MUC6* (gastric marker) and *CDX2* (intestinal marker).
1131
1132 **Supplementary Figure 4: Multi-omic profiling of a single cell-derived clonal organoid panel**
1133 **obtained from a dysplastic Barrett oesophagus PDO. (A)** VAF distributions across a single cell-
1134 derived clonal organoid panel (n=9) derived from a dysplastic PDO (AHM2392). Normal
1135 distributions around VAF=50% indicate clonality. **(B)** Tumour mutation burdens of the dysplastic-
1136 derived single cell-derived clonal organoid panel, with mutations classified as those shared with
1137 the bulk organoid from which they were derived, those not captured in the bulk organoid but
1138 present in at least one derived organoid, and private mutations. **(C)** Signature contributions
1139 across all mutations from the derived organoid panel, alongside adjacent tissue and bulk PDO
1140 obtained from the dysplastic and OAC tissues. **(D)** A phylogenetic profile of the PDO derived from
1141 AHM2392 defined using the derived organoid panel. Signature contributions were calculated
1142 across mutations contributing to each branch, respectively. Branch lengths are generally
1143 proportional to total amount of mutations. Signatures were not fitted for branches with fewer than
1144 25 SNVs. **(E)** Hierarchical clustering of RNA-seq profiling for the dysplasia single cell-derived
1145 clonal organoid panel using the top 500 variable genes following variance stabilised
1146 transformation of read counts. Heatmap annotation includes genetic alterations as reported in
1147 (F) and log2-transformed TPM-normalised counts of *MUC6* (a gastric marker) and *CDX2* (an
1148 intestinal markers). The green dotted lines in **(D)** and **(E)** represent matching clones according to
1149 the phylogenetic profiling and hierarchical clustering. **(F)** Driver alterations found across the
1150 dysplasia single cell-derived clonal organoid panel as well as bulk PDO and tissue derived from
1151 dysplasia and matched OAC tissue.
1152

1153 **Supplementary Figure 5: Morphological analysis of Barrett oesophagus PDOs. (A)**
1154 Representative bright-field images illustrating the three morphology classes visible in a
1155 dysplastic Barrett oesophagus PDO (AHM2221): single layer, single lumen; multiple layer, single
1156 lumen; and solid (multiple cells, no visible lumen). Lower panel shows coexistence of multiple
1157 morphologies within a single culture. Scale bars: 100 µm (top), 200 µm (bottom). **(B and C)** Size
1158 distribution of single cells identified in the non-dysplastic (AHM0040) and dysplastic (AHM2221)
1159 Barrett oesophagus PDO cultures. Histograms show counts per 1µm; dashed vertical line marks
1160 the mean cell diameter. PDOs were counted as a diameter of 21µm or greater. **(D)** Diameter
1161 distributions of measured non-dysplastic (AHM0040) PDOs stratified by morphology class and
1162 day (within each class, lighter to darker bars denote increasing time). Each subplot shows the
1163 frequency (proportion of organoids per bin) for that class/day. **(E)** Relationship between non-
1164 dysplastic (AHM0040) PDO size and proliferative activity. Boxplots show organoid diameter
1165 versus the number of nuclei scored per organoid, colour-coded by day (as labelled). Boxes
1166 indicate interquartile range, with the median value shown as the centre line. **(F)** Mean non-
1167 dysplastic (AHM0040) PDO area over time, separated by morphology (multiple lumen, blue;
1168 single lumen, red). **(G)** Adjacent non-dysplastic (AHM0040) PDO sizes measured at 196 hours and
1169 260 hours after seeding. Each point is one PDO; displacement from the diagonal reflects growth
1170 between time points. **(H)** Mean diameter-squared (proportional to number of cells) of single layer,
1171 single lumen organoids for non-dysplastic (AHM0040) and dysplastic (AHM2221) Barrett
1172 oesophagus organoids 4 and 6 days following seeding. **(I)** Time-lapse example of fusion in non-
1173 dysplastic (AHM0040) PDOs producing a single-layer, multi-lumen (SLML) morphology: at 196
1174 hours the two organoids are separate but by 204 hours they have fused; the fused organoid
1175 maintains an SLML morphology through 260 hours. **(J)** Example of a non-dysplastic (AHM0040)
1176 singe-layer single-lumen PDO interacting with and likely fusing with a single cell: in the fifth frame
1177 the single cell aligns with the organoid; in the sixth frame the single cell is no longer visible, and
1178 the organoid shows a thickened fluorescent region at the point of contact.
1179
1180 **Supplementary Figure 6: *In silico* modelling of PDO growth with variable polarity and**
1181 **polarity-inheritance. (A and B)** Overview of experimental quantification and *in silico* modelling
1182 of PDO morphology. **(A)** PDOs are imaged as z-stacks; the best-focused plane is outlined with an
1183 ellipse in Fiji and diameter is taken as the mean of minimum and maximum widths. PDOs are
1184 classified as single lumen, multi-lumen or solid; cell number is assumed to scale with diameter^2
1185 for hollow organoids and diameter^3 for solid PDOs **(B)** A 2D Cellular Potts model (CompuCell3D)
1186 simulates organoid cross-sections over Monte Carlo steps, illustrating growth, movement and

fusion over timepoints t0, t1, and t2. Each new PDO is assigned a polarity state according to an inherited polarity parameter, IP: IP=1 yields polarised, single-lumen, single-layer PDOs; IP >0 but <1 produces a mixture of lumen-forming and solid PDOs; and IP=0 produces non-polar, solid, non-luminal PDOs. Fusion events are favoured when the change in effective adhesion energy for increasing organoid–organoid contact is negative ($\Delta E_{fusion} < 0$). **(C)** Corresponding steady-state morphologies from the model: (i) a polarised PDO forming a single lumen and single epithelial layer (IP = 1), and (ii) a non-polar PDO developing as a solid, non-luminal structure (IP = 0). **(D)** Example of simulated PDO fusion: two separate single-lumen PDOs at an early time point (left) and the resulting fused multi-lumen PDO at a later time point (right). **(E)** Time course of a representative fusion event in the model, illustrating the approach, contact and remodelling of two solid PDOs into a single composite structure over successive Monte Carlo steps.

Supplementary Figure 7: Variation in transcriptional profiles across normal- and Barrett oesophagus-derived PDOs. (A) Comparisons of gastric and intestinal gene panel scores across the PDO cohort, calculated via gene set variation analysis on gene panels derived from the literature. **(B)** Unsupervised hierarchical clustering of PDOs using the top 1000 variable genes. Expression values underwent variance stabilising transformation followed by subtraction of the average expression for the respective gene. **(C)** Principal component analysis of Barrett oesophagus-derived PDOs alone. **(D and E)** Volcano plots displaying the results of differential expression analysis comparing (D) non-dysplastic and (E) dysplastic Barrett oesophagus-derived PDOs with normal gastric PDOs. Genes were coloured with relation to adjusted p-values less than 0.05 and absolute log2-fold change greater than 1. The 20 genes with the lowest adjusted p-values are annotated. **(F)** Functional enrichment analysis of up- and down-regulated DEGs specific to non-dysplastic PDOs. Full results are reported in **Supplementary Table 7**. **(G)** Functional enrichment analysis of up- and down-regulated DEGs specific to dysplastic PDOs. Full results are reported in **Supplementary Table 8**. **(H)** Comparisons of *HOXB5* and *HOXB7* gene expression across the PDO cohort. TPM-values were reported following log2-transformation. Gene expression was compared between non-dysplastic and dysplastic PDOs using a two-sample Wilcoxon test, adjusted for multiple testing using the Benjamini-Hochberg procedure.

Supplementary Figure 8: Assembloid co-cultures to explore clonal expansion.
(A) Schematic illustrating the assembloid culture system with fibroblasts under various in vitro conditions. **(B)** Brightfield and histopathological features of the assembloid cultures. Note the

similarity between Barrett oesophagus tissue (top right) and the corresponding assembloid (bottom right). **(C)** Flow cytometric analysis of fibroblasts and gating strategy. Proportion of $CD34^+$ S1 fibroblasts **(D)** and αSMA^+ S3 fibroblasts **(E)** within total fibroblasts in assembloids containing Barrett or gastric PDOs following treatment. **(F)** Schematic illustrating how clones capable of shaping a supportive niche and establishing a positive feedback loop are more likely to expand.

Supplementary Figure 9: Cytokine expression in Barrett oesophagus and oesophageal adenocarcinoma development.

Boxplots showing expression levels ($\log_2(1+TPM)$) of IL2, IFNG, IL4, IL5, IL6, IL10 and IL13 across normal gastric tissue, Barrett oesophagus (BO), and oesophageal adenocarcinoma (OAC). The data was derived from RNA-seq data from our previous study[51]. Note the significant increase in IL10.

Supplementary Figure 10: Genomic features of OAC PDOs and their relationship to parent tissue. (A and B) Correlation between tumour purity for PDOs and their adjacent tissues. Purity between PDO-tissue pairs was calculated via a pairwise Wilxocon test. **(C)** Tumour mutational burden in PDOs and their adjacent tissues. **(D)** Differences in VAFs of shared mutations across PDO-tissue pairs, with the dotted red-line indicating mutations where $VAF_{organoid} - VAF_{tissue} = 0$ (i.e. where a mutation has equal VAF in a PDO and its adjacent tissue). **(E)** Comparison of insertion-deletion (indel) mutation burden between PDOs and their adjacent tissues. **(F)** Comparison of SNV burden between PDOs and their adjacent tissues. **(G)** Comparison of ploidy in PDOs and their adjacent tissues. **(H)** Comparison of HRD index score in PDOs and their adjacent tissues. **E-H)** Red dots indicate PDO-tissue pairs with mutational concordance less than 10% and gray dots indicate PDO-tissue pairs with mutational concordance more than 10%, as reported in **Figure 5C**. Red dotted lines indicate equivalent values (i.e. y=x). Solid blue lines and shaded grey areas indicate linear regression lines of best fit alongside 95% confidence bands. Solid navy lines indicate linear regression lines following the removal of PDO-tissue pairs with mutational concordance less than 10%. Comparisons were made using Pearson correlation coefficients with R- and p- values shown. Values shown in black in the top left were calculated across all PDO-tissue pairs, and values shown in navy in the bottom right were calculated following the removal of PDO-tissue pairs with mutational concordance less than 10%. **(I)** Summary of mutational signature analysis on adjacent OAC PDOs and their parent tissues. Samples (rows) are ordered into matched PDO-tissue pairs. **(J)** Correlations in SBS17a (left) and SBS17b (right) contributions

across PDO-tissue pairs with Pearson correlation coefficients calculated separately for SBS17a and SBS17b. Annotations are the same as in (E to H). **(K)** Contributions of mutational signatures across both the gastric/BO and OAC PDO cohorts. **(L and M)** Gene set enrichment analysis of the loadings for (L) PC1 and (M) PC2 obtained from principal component analysis of RNA-seq data from the OAC PDO cohort. Analysis was based on the top 1000 variable genes across the cohort.

Supplementary Figure 11: Circos plots demonstrating genomic similarities between each OAC PDO and its parent tissue. Each plot demonstrates overall genomic landscape of the organoid (O) and adjacent tumour tissue (T). The outer circle represents the labelled chromosomes with labelled driver gene positions. The middle circle depicts copy number profile where orange shows gains and blue shows deletions. The inner most circle shows inter and intra chromosomal structural variations with grey, red, blue and green lines representing translocations, deletions, inversions and duplications, respectfully.

Supplementary Figure 12: Immunohistochemistry and fluorescence *in situ* hybridisation of *HER2*.

Supplementary Figure 13: Morphological analysis of OAC PDOs. (A) Representative bright-field images illustrating the three morphology classes visible in an OAC PDO (CAM277): single layer, single lumen; multiple layer, single lumen; solid. Image taken at day 4. Scale bar shows 100µm. **(B)** Coexistence of multiple morphologies at day 7 of a single CAM277 culture. Scale bar shows 100µm. **(C)** Size distribution of single cells identified in a single CAM277 OAC PDO culture. Histogram shows counts per 1µm interval; dashed vertical line marks mean cell diameter. PDOs were counted as a diameter of 21µm or greater. **(D)** Size of OAC PDO (CAM277) single cells compared with Barrett oesophagus non-dysplastic (AHM0040) and dysplastic (AHM2221) PDOs. Statistical comparisons made using the Kruskal-Wallis test. **(E)** Distribution of CAM277 PDO size at days 4, 6 and 7 after seeding. **(F)** Correlation between growth at 72 hours and growth at 140 hours for 76 individual CAM277 organoids. **(G)** Representative brightfield image demonstrating fusion of two solid CAM277 organoids between 72 and 140 hours of seeding (images taken at four hourly intervals from top left through to bottom right).

Supplementary Figure 14: Decision framework for classifying precancerous organoids. Decision tree showing how patient-derived organoids are classified by integrating patient disease grade, matching tissue, *TP53* status, mutation burden, and genomic instability. The framework

emphasizes tissue-anchored, multi-modal interpretation rather than single-feature classification, and mainly to distinguish normal gastric and precancerous organoids in BO.

LIST OF TABLES

Patient ID	Age	Sex	Ethnicity	Highest grade recorded	IM present	Adjacent to OAC	Clinical trajectory after derivation
AHM0040	69	M	White British	NDBO	Y	N	Non-progressor
AHM0931	73	M	White British	NDBO	Y	N	Non-progressor
AHM1345	71	F	White British	NDBO	Y	N	Non-progressor
AHM1369	80	M	White British	NDBO	Y	N	Non-progressor
AHM1678	79	M	White British	NDBO	Y	N	Non-progressor
AHM1977	68	F	White British	NDBO	Y	N	Non-progressor
AHM2172	73	F	White British	NDBO	Y	N	Non-progressor
AHM2575	79	F	White British	NDBO	N	N	Non-progressor
AHN0070	83	M	White British	NDBO	Y	N	Non-progressor
AHM1373	74	M	White British	NDBO	Y	N	Non-progressor
AHM2149	67	M	White British	NDBO	Y	N	Non-progressor
CAM673	66	M	White British	NDBO	Y	N	No recurrence
CAM478	61	M	White British	LGD	Y	Y	No recurrence
CAM478	61	M	White British	HGD	N	Y	No recurrence
CAM603	74	M	White British	HGD	Y	Y	Non-progressor
AHM2165	77	M	White British	HGD	N	Y	No recurrence
AHM2221	74	F	White British	HGD	N	Y	Non-progressor
AHM2392	87	F	White British	HGD	-	N	Progressor
AHM2688	73	M	White British	NDBO	-	N	Non-progressor

Table 1: Demographic and clinicopathological characteristics of donors for PDOs obtained from non-dysplastic and dysplastic Barrett oesophagus. - missing data. F, female; HGD, high grade dysplasia; IM, intestinal metaplasia; M, male; LGD, low grade dysplasia; NDBO, non-dysplastic Barrett oesophagus; OAC, oesophageal adenocarcinoma.

ID	Source	Age	Sex	Surgical TNM	Chemotherapy regimen	Histopathological grading	TRG score
CAM473	Resection	78	M	T3N0Mx	ECX	Poor	3
CAM621	Resection	57	M	T1bN1M0	ECX	Poor	3
CAM453	Staging Lap	69	M	T3N1M0	ECX	Poor	4
CAM453	Resection	69	M	T3N1M0	ECX	Poor	4
CAM296	Resection	72	M	T3N3Mx	ECF	Poor	4
CAM486	Resection	72	M	T4aN0M0	ECX	Moderate	4
CAM540	Resection	52	M	T3N0M0	ECX	Poor	4
CAM535	Resection	72	F	T3N1M0	ECX	Poor	4
CAM522	Resection	62	M	T4aN1M0	ECX	Poor	4
CAM247	Resection	67	M	T2N2M0	ECX	Moderate	4
CAM292	Resection	66	F	T3N1Mx	ECX	Poor	4
CAM388	Resection	78	M	T2N0M0	ECX	Poor	4
CAM429	Resection	77	M	T2N0M0	ECX	Moderate	4
CAM479	Resection	63	M	T3N0M0	ECX	Poor	4
CAM433	Resection	66	M	T3N2M0	ECX	Poor	4
CAM629	Resection	61	M	T3N1M0	FLOT	Moderate	4
CAM664	Resection	62	M	T3N0M0	FLOT	Moderate	4
CAM665	Resection	61	F	T3N3M0	FLOT	Poor	4
CAM668	Resection	57	M	T3N3M0	FLOT	Poor	4
CAM676	Resection	59	M	T3N1M0	FLOT	Poor	4
CAM401	Resection	77	F	T4aN2M0	CF	Poor	5
CAM467	Resection	68	M	T2N0M0	ECX	Poor	5
CAM542	Resection	77	M	T3N2M0	ECX	Poor	5
CAM338	Resection	51	F	T3N1Mx	ECX	Poor	5
CAM423	Resection	55	M	T3N2M0	ECX	Poor	5
CAM446	Resection	68	F	T4aN3M0	ECX	Poor	5
CAM576	Resection	51	M	T4bN1	FLOT	Poor	5
CAM614	Resection	76	M	T4aN3M0	FLOT	Moderate	5
CAM667	Resection	62	M	T3N3M0	FLOT	Moderate	5
CAM421	Staging Lap	57	M	-	CF	Poor	Not available*
CAM408	Resection	60	M	T1aN0M0	None	Moderate	n/a
CAM412	Resection	51	F	T1bN0M0	None	Poor	n/a
CAM450	Resection	76	M	T1N0M0	None	Moderate	n/a
CAM471	Resection	82	M	T3N3M0	None	Poor	n/a
CAM277	Resection	80	F	T3N2M0	None	Poor	n/a
CAM501	Staging Lap	72	M	T3N2M0	ECX	Moderate	n/a
CAM574	Resection	71	M	T3N1M0	None	Moderate	n/a
OESO117	Unknown	61	M	T3 N2 M0	None	-	n/a
OESO146	Unknown	73	M	T2 N0 M0	None	-	n/a

Table 2: Demographic and clinicopathological characteristics of organoids derived from patients with oesophageal adenocarcinoma. All patients were White British. *TRG not available but sample noted demonstrate therapy-related tumour regression. - missing data. ECX, epirubicin, cisplatin, capecitabine; CF, cisplatin, 5-fluorouracil; FLOT: 5-fluorouracil/leucovorin, oxaliplatin, docetaxel; Lap laparoscopy; TRG, tumour regression grade.

Features / dimensions	Normal gastric organoids	Non-dysplastic BO organoids	Dysplastic BO organoids	OAC organoids
Driver gene mutations	No enrichment for OAC-selected driver events; absence of TP53 and CDKN2A alterations typical of Barrett progression	Frequent *CDKN2A* or ARID1A alterations; TP53 generally absent or subclonal	*TP53* alterations common but could be absent; *CDKN2A* or *ARID1A* frequently co-altered, or progression-associated events	High frequency of *TP53* mutations; recurrent copy number alterations affecting *CDKN2A, ARID1A, GATA6, SMAD4* and others
Genome-wide features	Very low mutation burden; no evidence of chromosomal instability or whole-genome doubling	Intermediate mutation burden (usually > 2/Mb); mutational signatures concordant with Barrett tissue even when SNV overlap is low	Higher mutation burden (usually > 4/Mb); increased genomic instability	Copy-number alterations dominate; high chromosomal instability and frequent whole-genome doubling
Transcriptome / lineage state	Strong gastric lineage program (e.g. gastric mucins, digestive enzyme genes); minimal intestinal signature. Separated from BO organoids in PCA analysis	Mixed gastric–intestinal state; inverse relationship between gastric and intestinal programs; Separated from gastric organoids in PCA analysis	Separated from gastric organoids in PCA analysis; increased expression of *HOX* genes relative to non-dysplastic BO	Diverse tumour transcriptional states; no single uniform OAC program
Morphology & growth kinetics	Benign glandular morphology; used as baseline rather than growth comparison	Four morphologies: single-layer single-lumen; single-layer multi-lumen; multi-layer luminal; solid. Luminal types expand more robustly	Loss of single-layer multi-lumen morphology; increased proportion of solid organoids	Predominantly solid morphology; cell fusion events contribute to growth variability

Table 3: Integrated framework for classifying Barrett oesophagus and oesophageal adenocarcinoma organoids. A decision-based framework to distinguish normal gastric and precancerous organoids are also described in **Supplementary Figure 14.**

LIST OF SUPPLEMENTARY TABLES

<Separate file>

Supplementary Table 1: Metadata relating to archived data for models generated in this study.

Individual ID	Age	Sex	Organoid derived from	Condition/Procedure
DE04	63	Male	GOJ	Gastrointestinal disease-free organ donor
DE26	61	Female	GOJ	Gastrointestinal disease-free organ donor
DE26	61	Female	Gastric body	Gastrointestinal disease-free organ donor
DE27	35	Male	GOJ	Gastrointestinal disease-free organ donor
DE27	35	Male	Gastric body	Gastrointestinal disease-free organ donor
DE28	37	Male	GOJ	Gastrointestinal disease-free organ donor
DE28	37	Male	Gastric body	Gastrointestinal disease-free organ donor
MS050	63	Male	Jejunum	Gastrectomy
HGH046	67	Female	Jejunum	Gastrectomy
TB16.0980	42	Male	Duodenum	Pancreaticoduodenectomy

Supplementary Table 2: A summary of demographic and clinicopathological characteristics of donors of control intestinal and gastric organoids. GOJ: gastroesophageal junction.

Day	Measure	Single layer, single lumen	Single layer, multi-lumen	Multi-layer, with lumen	Solid, multiple cells
4	Number of organoids (%)	769 (53%)	343 (23%)	139 (9%)	213 (15%)
	Max diameter (µm)	378	380	160	84.0
	Mean diameter (µm)	85.2	94.7	46.3	27.1
	Mean circularity	1.11	1.12	1.08	1.06
6	Number of organoids (%)	720 (58%)	326 (26%)	68 (6%)	119 (10%)
	Max diameter (µm)	513	397	213	83.3
	Mean diameter (µm)	106	121	63.1	27.0
	Mean circularity	1.12	1.15	1.08	1.06
7	Number of organoids (%)	776 (61%)	322 (25%)	60 (5%)	117 (9%)
	Max diameter (µm)	376	421	143	104
	Mean diameter (µm)	108	129	64.3	27.3
	Mean circularity	1.13	1.15	1.10	1.07

Supplementary Table 3: Morphological characteristics of a non-dysplastic Barrett oesophagus PDO (AHM0040) at four, six and seven days following seeding.

Day	Measure	Single layer, single lumen	Multi-layer, with lumen	Solid, multiple cells
4	Number of organoids	153 (29%)	142 (27%)	245 (45%)
	Max diameter (µm)	202	91.9	135
	Mean diameter (µm)	72.8	52.2	43
	Mean circularity	1.08	1.07	1.07
6	# organoids (%)	241 (34%)	212 (30%)	255 (36%)
	Max diameter (µm)	444	250	187
	Mean diameter (µm)	93.5	64.2	52.7
	Mean circularity	1.12	1.08	1.07

Supplementary Table 4: Morphological characteristics of a dysplastic Barrett oesophagus PDO (AHM2221) at four, six and seven days following seeding.

	Single layer, single lumen	Single layer, multi-lumen	Multi-layer, with lumen	Solid
***In vitro* observations (>1% organoids)**	BO lines only (AHM0040, AHM2221)	NBDO only (AHM0040)	BO lines only (AHM0040, AHM2221)	BO and OAC (AHM0040, AHM2221, CAM277)
***In Silico* observations**	Single organoids	Fused SLSL organoids	Single organoids	Single and fused organoids
Parameters	IP = 1 EP = True	As for SLSL	IP<1, IP>0 EP = True	IP 0 or EP False
Parameter interpretation	Cells all polar	Cells all polar	Some cells with disrupted polarity	Cells all with disrupted polarity

1351

1352 **Supplementary Table 5: Summary of *in silico* and *in vitro* observations for the growth**
1353 **patterns and morphology of non-dysplastic (AHM0040) and dysplastic (AHM2221) Barrett**
1354 **oesophagus PDOs.** BO, Barrett oesophagus; EP, establish polarity (i.e. whether cells are polar);
1355 IP, inherit polarity (i.e. the likelihood of a cell inheriting polarity); NBDO, non-dysplastic Barrett
1356 oesophagus; OAC, oesophageal adenocarcinoma; SLSL, single layer, single lumen.

1357

<Separate file>

Supplementary Table 6: a summary of enriched processes and pathways relating to genes that are differentially expressed only non-dysplastic and dysplastic Barrett oesophagus versus gastric patient derived organoids. BP: biological process; GO: gene ontology; MF: molecular function; TF: transcription factor; WP: Wiki pathway.

<Separate file>

Supplementary table 7: a summary of enriched processes and pathways relating to genes that are differentially expressed only in non-dysplastic Barrett oesophagus versus gastric patient derived organoids. BP: biological process; GO: gene ontology; MF: molecular function; TF: transcription factor; WP: Wiki pathway.

<Separate file>

Supplementary table 8: a summary of enriched processes and pathways relating to genes that are differentially expressed only in dysplastic versus gastric patient derived organoids. BP: biological process; GO: gene ontology; MF: molecular function; TF: transcription factor; WP: Wiki pathway.

Solid organoids	Day 4	Day 6	Day 7
Number of organoids	1936	2013	1918
Mean diameter (µm)	43.2	47.9	49.2
Maximum diameter (µm)	183	262	213
Mean circularity	1.07	1.07	1.08
Proportion of solid organoids	99%	99%	99%

Supplementary Table 9: Morphological characteristics of an OAC PDO (CAM277) at four, six and seven days following seeding.

	5FU+ Leucovorin			Oxaliplatin			Docetaxel		
	IC50	**AUC**	**Emax**	**IC50**	**AUC**	**Emax**	**IC50**	**AUC**	**Emax**
CAM574	19.12	206.7	95.2	19.65	242.1	92.7	1.41	149.2	78.0
CAM277	8.50	179.9	94.6	9.24	174.8	96.2	2.04	185.3	70.4
CAM408	56.25	254.5	95.8	74.32	295.6	69.7	3.04	161.5	72.9
CAM117	13.60	186.0	96.1	93.57	273.8	81.2	2.69	132.7	93.5
CAM146	21.95	197.9	82.4	25.65	234.6	73.1	1.89	211.5	48.7

Supplementary Table 10: OAC PDO sensitivity to cytotoxic chemotherapy. AUC: area under the curve (an integral value of viability following exposure to defined concentrations of each drug); E_{max}: the maximum effect; IC_{50}: the concentration of each drug required to reduce viability to 50%; 5FU: 5-fluorouracil.

	CAM277	CAM401	CAM408	CAM412	CAM429	CAM501	CAM535	CAM574
0 Gy	1	1	1	1	1	1	1	1
2 Gy	0.86	0.88	1.03	0.77	0.71	0.42	0.58	0.62
4 Gy	0.80	0.62	0.99	0.56	0.66	0.54	0.57	0.78
6 Gy	0.74	0.77	1.10	0.52	0.53	0.36	0.59	0.70
8 Gy	0.68	0.75	0.73	0.62	0.60	0.24	0.47	0.55
AUC	0.83	0.79	0.98	0.66	0.67	0.46	0.63	0.70

Supplementary Table 11: OAC PDO sensitivity to x-ray irradiation. Organoid forming efficiency shown for each PDO following exposure to 0-8Gy x-ray irradiation in a single fraction. AUC, median area under the curve (integral of 0-8Gy organoid forming efficiency values).

Organoid	IC_{50} (geometric mean, μM)	IC_{50} (range, μM)	Observed E_{max} (mean, %)	Observed E_{max} (range, %)	AUC
CAM277	0.908	0.9–0.916	70	60.9–79.0	332.4
CAM401	2.87	2.39–3.44	35.7	24.2–47.3	379.7
CAM429	0.586	0.519–0.663	48.6	43.2–53.9	349.6
CAM535	1.302	0.729–2.33	48.9	27.3–70.4	356

Supplementary Table 12: OAC PDO sensitivity to the CDK4/6 inhibitor abemaciclib. AUC: area under the curve (an integral value of viability following exposure to defined concentrations of each drug); E_{max}: the maximum effect; IC_{50}: the concentration of each drug required to reduce viability to 50%.

Figure 1

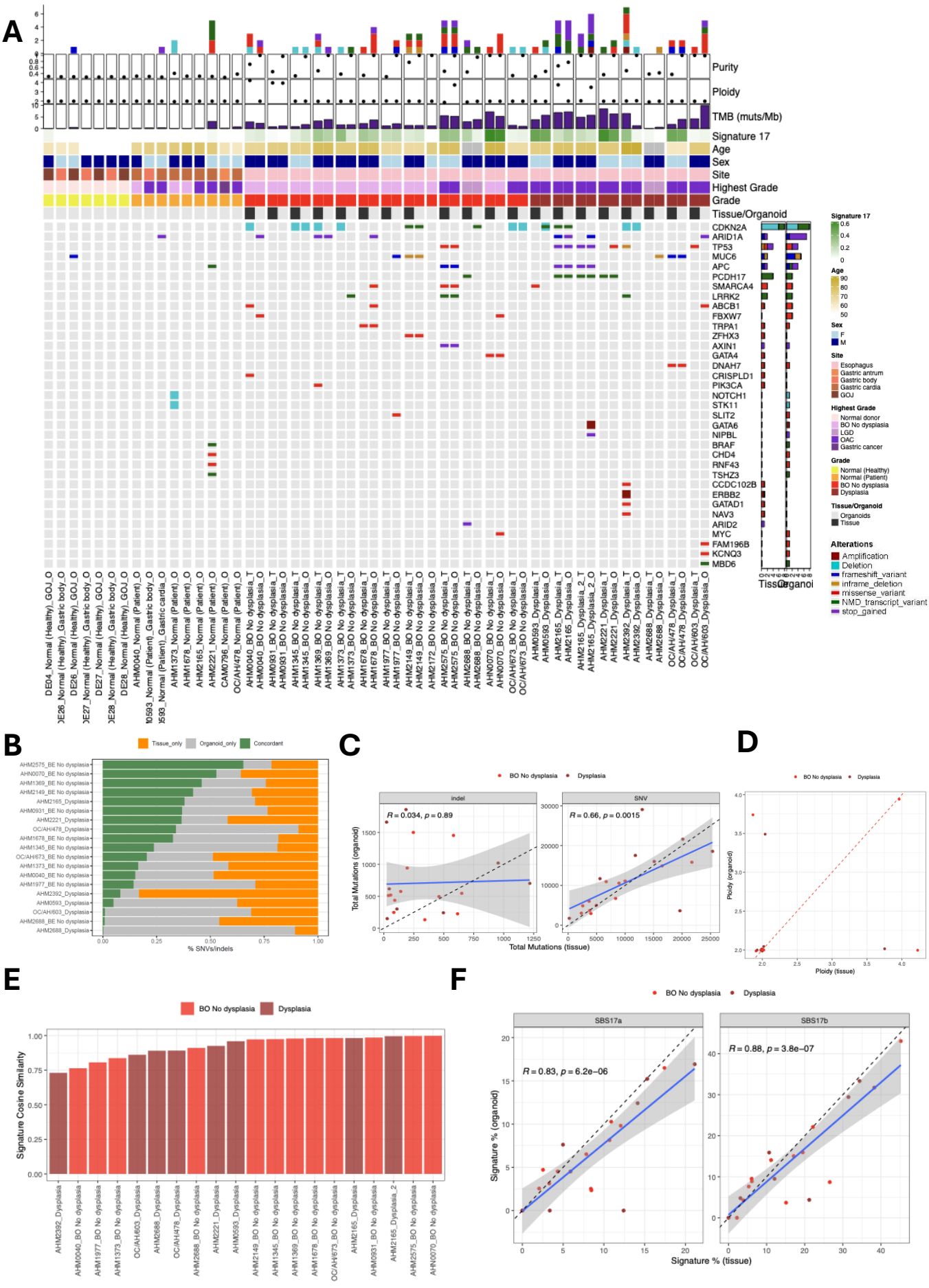
A
Purity
Ploidy
TMB (muts/Mb)
Signature 17
Age
Sex
Site
Highest Grade
Grade
Tissue/Organoid
CDKN2A
ARID1A
TP53
MUC6
APC
PCDH17
SMARCA4
LRRK2
ABCB1
FBXW7
TRPA1
ZFHX3
AXIN1
GATA4
DNAH7
CRISPLD1
PIK3CA
NOTCH1
STK11
SLIT2
GATA6
NIPBL
BRAF
CHD4
RNF43
TSHZ3
CCDC102B
ERBB2
GATAD1
NAV3
ARID2
MYC
FAM196B
KCNQ3
MBD6
Tissue
Organoid
Signature 17
Age
Sex
F
M
Site
Esophagus
Gastric antrum
Gastric body
Gastric cardia
GOJ
Highest Grade
Normal donor
BO No dysplasia
LGD
OAC
Gastric cancer
Grade
Normal (Healthy)
Normal (Patient)
BO No dysplasia
Dysplasia
Tissue/Organoid
Organoids
Tissue
Alterations
Amplification
Deletion
frameshift_variant
inframe_deletion
missense_variant
NMD_transcript_variant
stop_gained
B
Tissue_only
Organoid_only
Concordant
% SNVs/indels
C
BO No dysplasia
Dysplasia
indel
SNV
R = 0.034, p = 0.89
R = 0.66, p = 0.0015
Total Mutations (organoid)
Total Mutations (tissue)
D
BO No dysplasia
Dysplasia
Ploidy (organoid)
Ploidy (tissue)
E
BO No dysplasia
Dysplasia
Signature Cosine Similarity
F
BO No dysplasia
Dysplasia
SBS17a
SBS17b
R = 0.83, p = 6.2e−06
R = 0.88, p = 3.8e−07
Signature % (organoid)
Signature % (tissue)

Figure 2

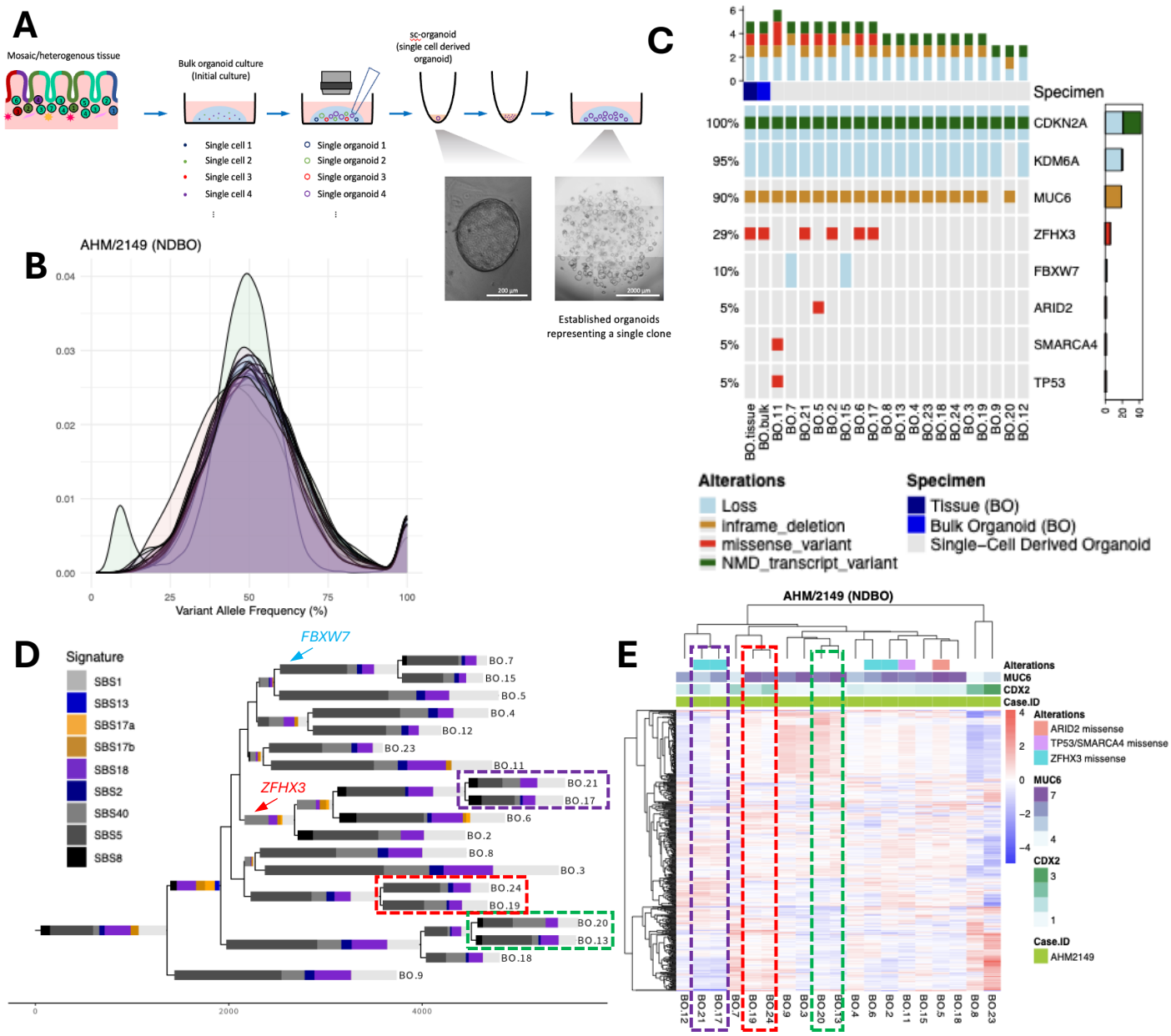
A
Mosaic/heterogenous tissue
Bulk organoid culture
(Initial culture)
sc-organoid
(single cell derived
organoid)
Single cell 1
Single cell 2
Single cell 3
Single cell 4
Single organoid 1
Single organoid 2
Single organoid 3
Single organoid 4
Established organoids
representing a single clone
B
AHM/2149 (NDBO)
Variant Allele Frequency (%)
C
Specimen
CDKN2A
KDM6A
MUC6
ZFHX3
FBXW7
ARID2
SMARCA4
TP53
Alterations
Loss
inframe_deletion
missense_variant
NMD_transcript_variant
Specimen
Tissue (BO)
Bulk Organoid (BO)
Single-Cell Derived Organoid
D
Signature
SBS1
SBS13
SBS17a
SBS17b
SBS18
SBS2
SBS40
SBS5
SBS8
FBXW7
ZFHX3
E
AHM/2149 (NDBO)
Alterations
MUC6
CDX2
Case.ID
ARID2 missense
TP53/SMARCA4 missense
ZFHX3 missense
AHM2149

Figure 3

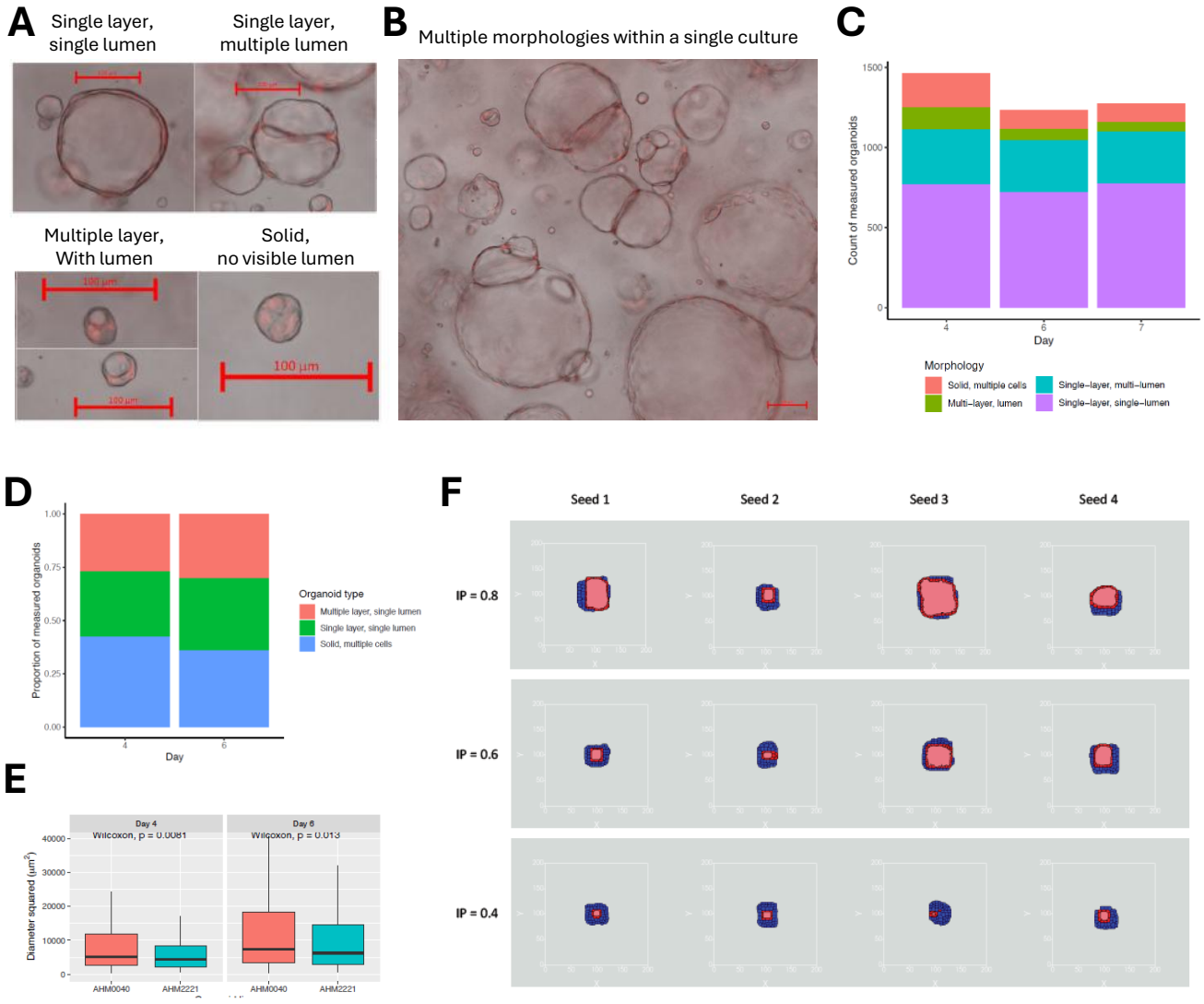
A
Single layer, single lumen
Single layer, multiple lumen
Multiple layer, With lumen
Solid, no visible lumen
100 µm
B
Multiple morphologies within a single culture
C
Count of measured organoids
Day
Morphology
Solid, multiple cells
Multi-layer, lumen
Single-layer, multi-lumen
Single-layer, single-lumen
D
Proportion of measured organoids
Day
Organoid type
Multiple layer, single lumen
Single layer, single lumen
Solid, multiple cells
E
Day 4
Wilcoxon, p = 0.0081
Day 6
Wilcoxon, p = 0.013
Diameter squared (µm²)
AHM0040
AHM2221
F
Seed 1
Seed 2
Seed 3
Seed 4
IP = 0.8
IP = 0.6
IP = 0.4

Figure 4

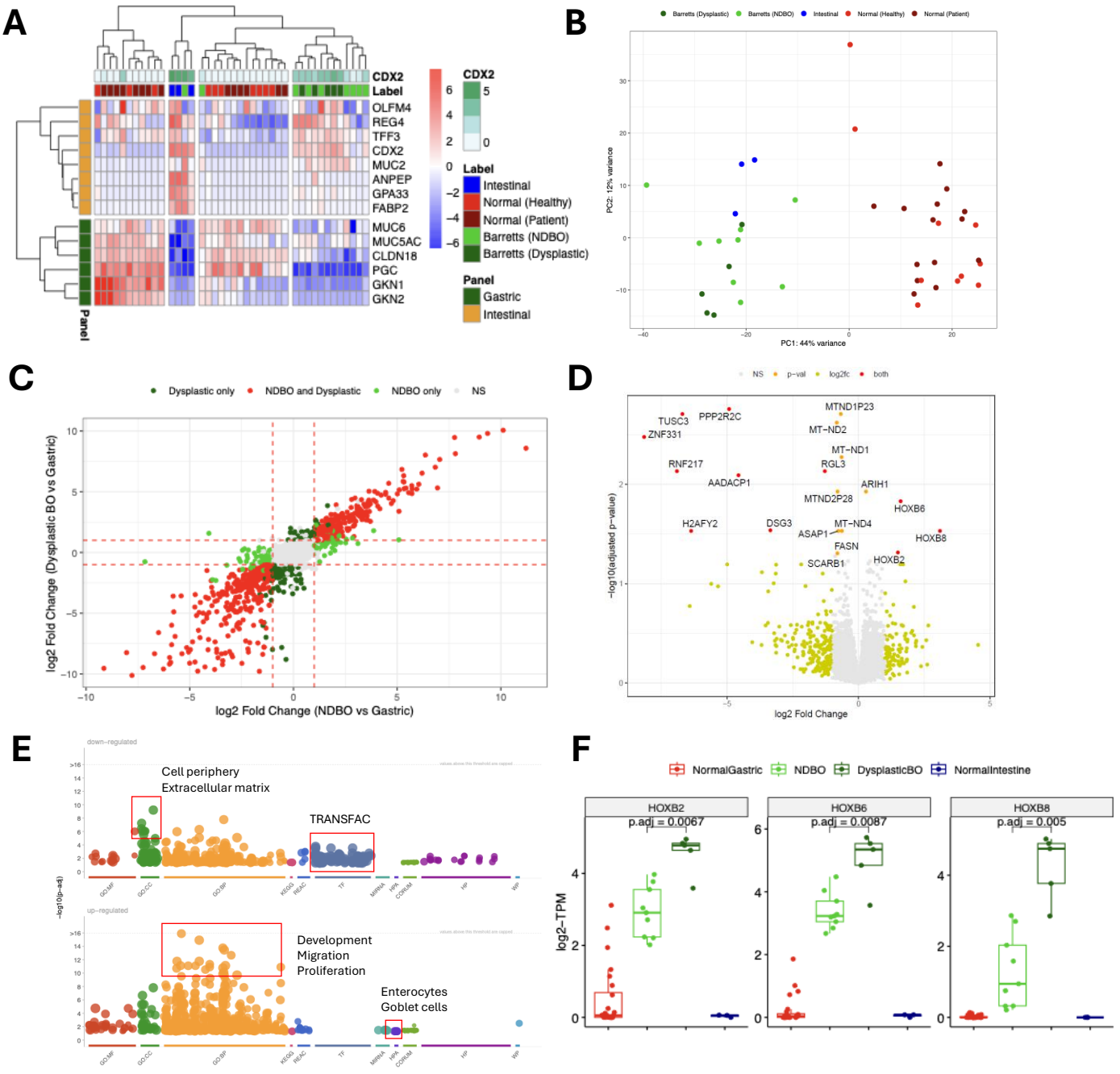
A
CDX2
Label
OLFM4
REG4
TFF3
CDX2
MUC2
ANPEP
GPA33
FABP2
MUC6
MUC5AC
CLDN18
PGC
GKN1
GKN2
Panel
Intestinal
Normal (Healthy)
Normal (Patient)
Barretts (NDBO)
Barretts (Dysplastic)
Gastric
B
Barretts (Dysplastic)
Barretts (NDBO)
Intestinal
Normal (Healthy)
Normal (Patient)
PC2: 12% variance
PC1: 44% variance
C
Dysplastic only
NDBO and Dysplastic
NDBO only
NS
log2 Fold Change (Dysplastic BO vs Gastric)
log2 Fold Change (NDBO vs Gastric)
D
NS
p-val
log2fc
both
MTND1P23
TUSC3
PPP2R2C
ZNF331
MT-ND2
MT-ND1
RNF217
RGL3
AADACP1
ARIH1
MTND2P28
HOXB6
H2AFY2
DSG3
MT-ND4
ASAP1
HOXB8
FASN
SCARB1
HOXB2
−log10(adjusted p-value)
log2 Fold Change
E
down-regulated
Cell periphery
Extracellular matrix
TRANSFAC
up-regulated
Development
Migration
Proliferation
Enterocytes
Goblet cells
F
NormalGastric
NDBO
DysplasticBO
NormalIntestine
HOXB2
p.adj = 0.0067
HOXB6
p.adj = 0.0087
HOXB8
p.adj = 0.005
log2−TPM

Figure 5

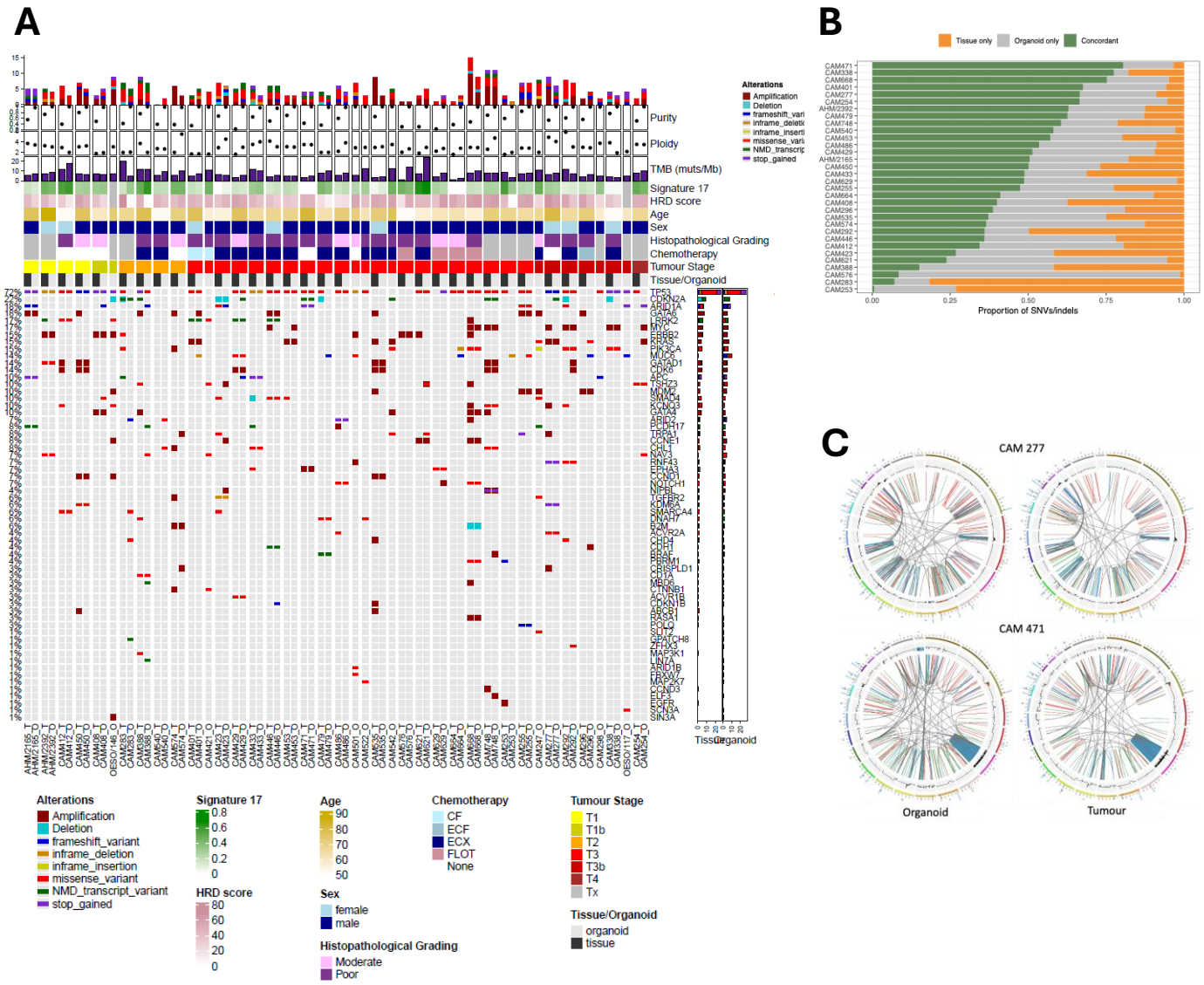
A
Purity
Ploidy
TMB (muts/Mb)
Signature 17
HRD score
Age
Sex
Histopathological Grading
Chemotherapy
Tumour Stage
Tissue/Organoid
Alterations
Amplification
Deletion
frameshift_variant
inframe_deletion
inframe_insertion
missense_variant
NMD_transcript_variant
stop_gained
Tissue
Organoid
B
Tissue only
Organoid only
Concordant
Proportion of SNVs/indels
C
CAM 277
CAM 471
Organoid
Tumour
Signature 17
HRD score
Sex
female
male
Histopathological Grading
Moderate
Poor
Chemotherapy
CF
ECF
ECX
FLOT
None
Tumour Stage
T1
T1b
T2
T3
T3b
T4
Tx
Tissue/Organoid
organoid
tissue

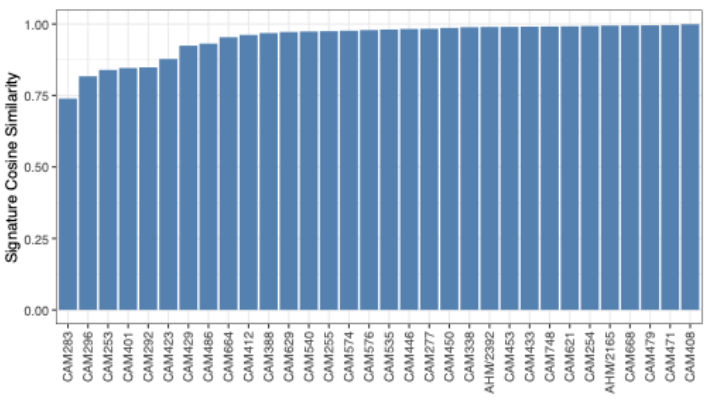
D
Signature Cosine Similarity
1.00
0.75
0.50
0.25
0.00
CAM283
CAM296
CAM253
CAM401
CAM292
CAM423
CAM429
CAM486
CAM664
CAM412
CAM388
CAM629
CAM540
CAM255
CAM574
CAM576
CAM535
CAM446
CAM277
CAM450
CAM338
AHM2392
CAM453
CAM433
CAM748
CAM621
CAM254
AHM2165
CAM668
CAM479
CAM471
CAM408

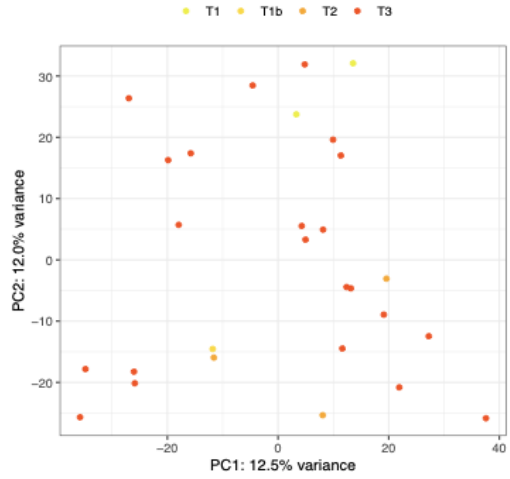
E
T1
T1b
T2
T3
PC2: 12.0% variance
PC1: 12.5% variance
30
20
10
0
−10
−20
−20
0
20
40

Figure 6

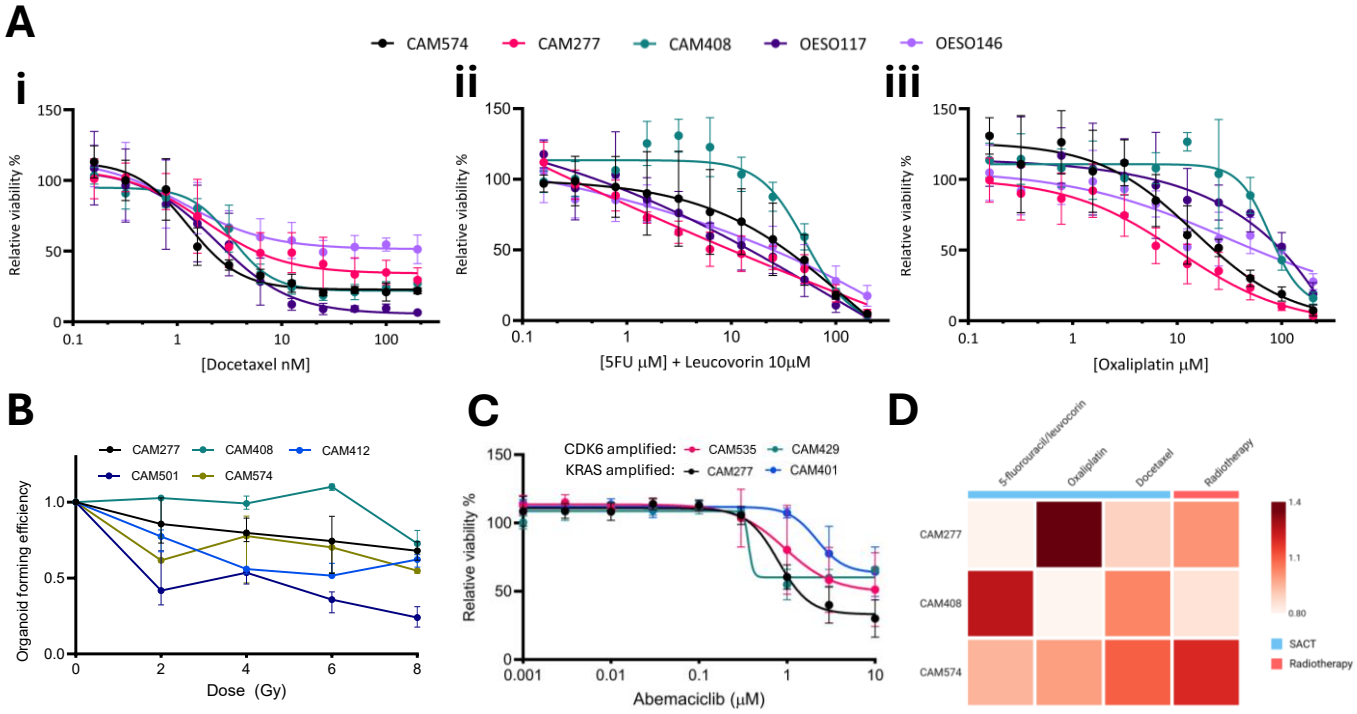
A
CAM574
CAM277
CAM408
OESO117
OESO146
i
ii
iii
Relative viability %
[Docetaxel nM]
[5FU µM] + Leucovorin 10µM
[Oxaliplatin µM]
B
CAM277
CAM408
CAM412
CAM501
CAM574
Organoid forming efficiency
Dose (Gy)
C
CDK6 amplified:
KRAS amplified:
CAM535
CAM429
CAM277
CAM401
Relative viability %
Abemaciclib (µM)
D
5-fluorouracil/leucovorin
Oxaliplatin
Docetaxel
Radiotherapy
CAM277
CAM408
CAM574
SACT
Radiotherapy

Supplementary Figure 1

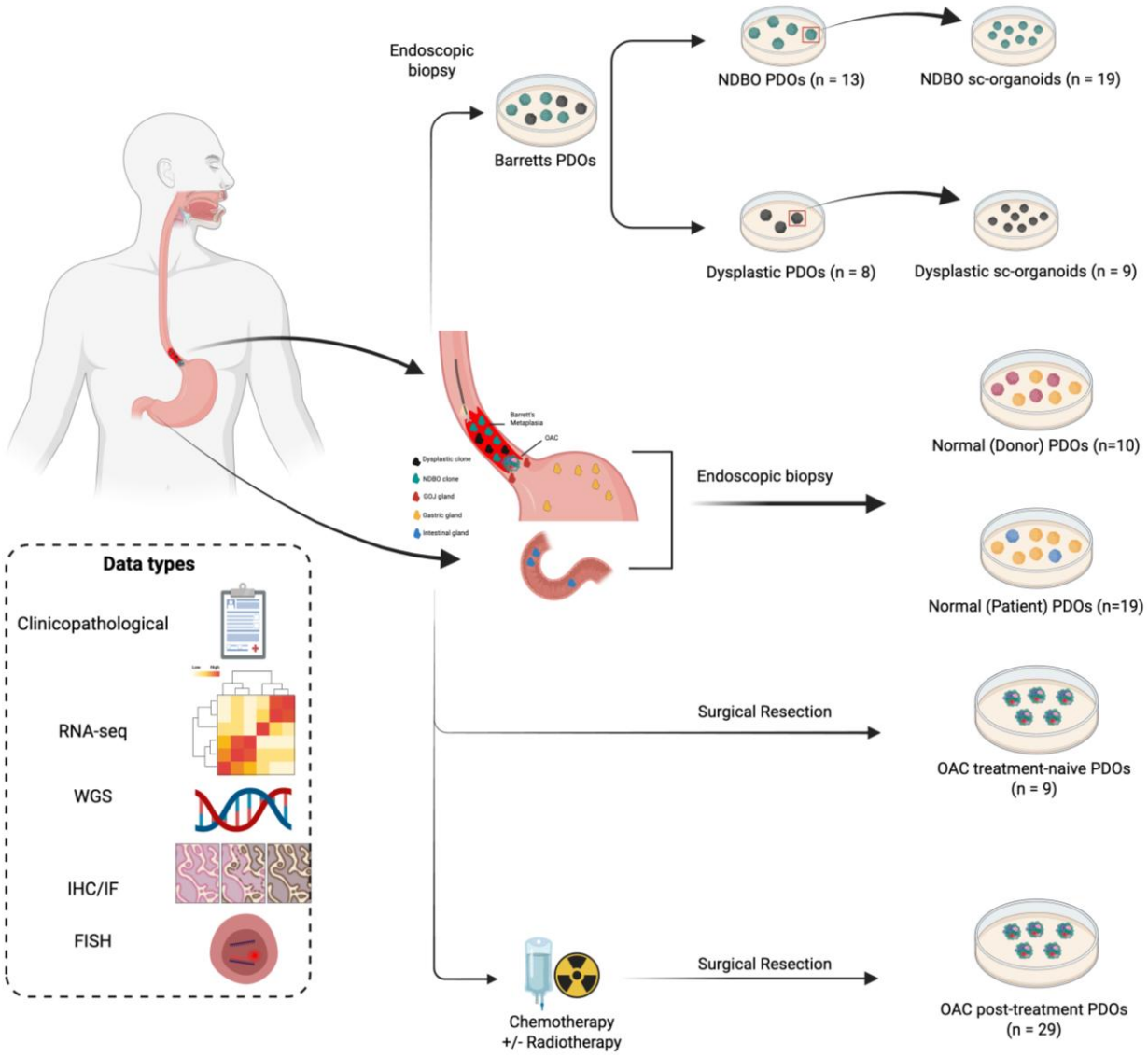

Supplementary Figure 2

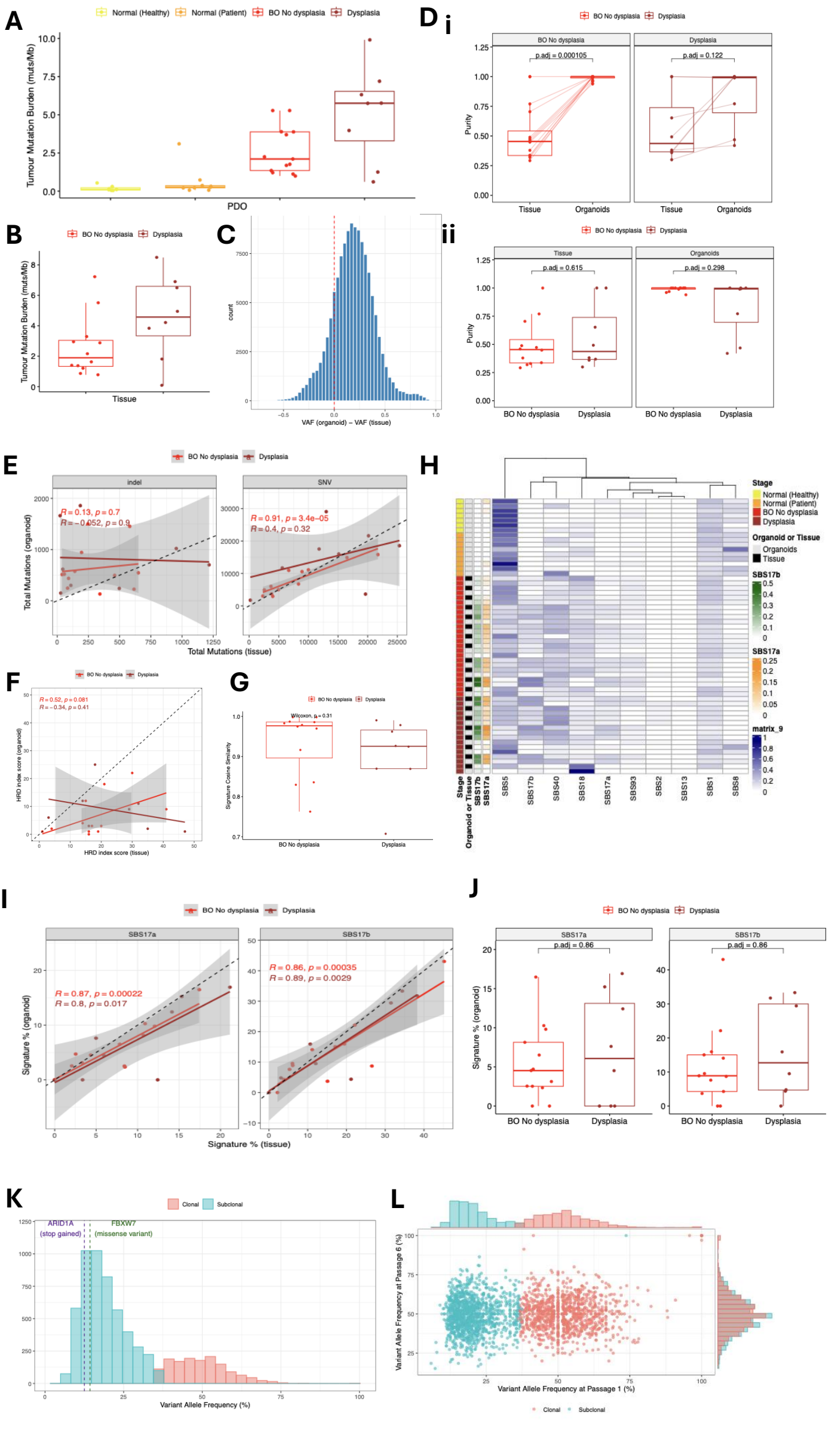

Supplementary Figure 3

A

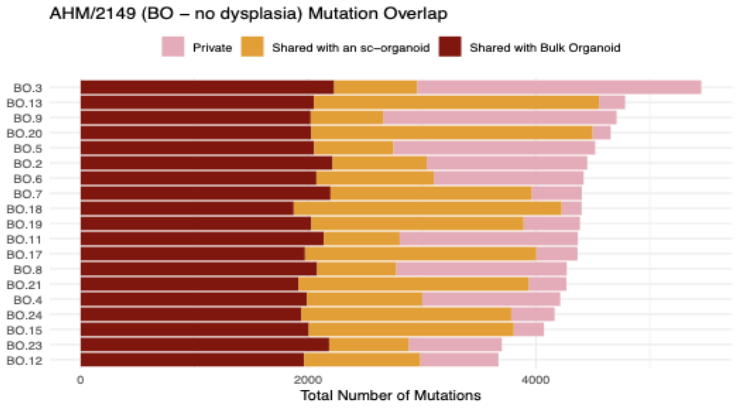

B

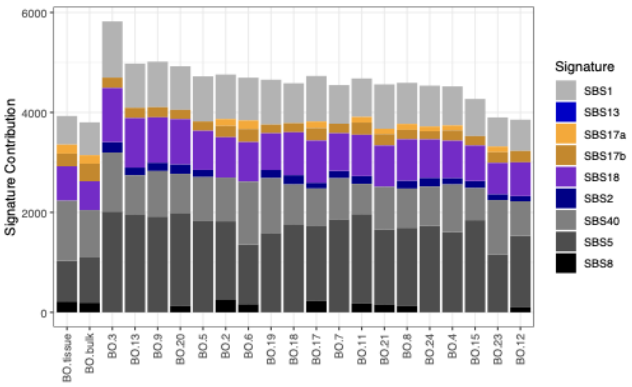

C

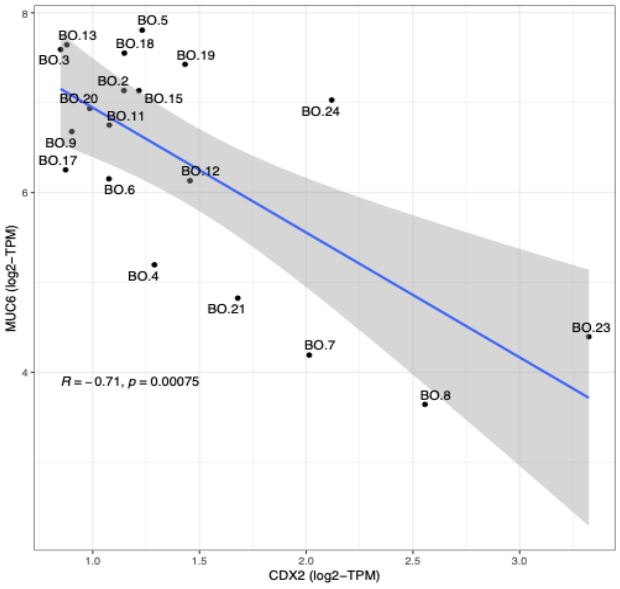

Supplementary Figure 4

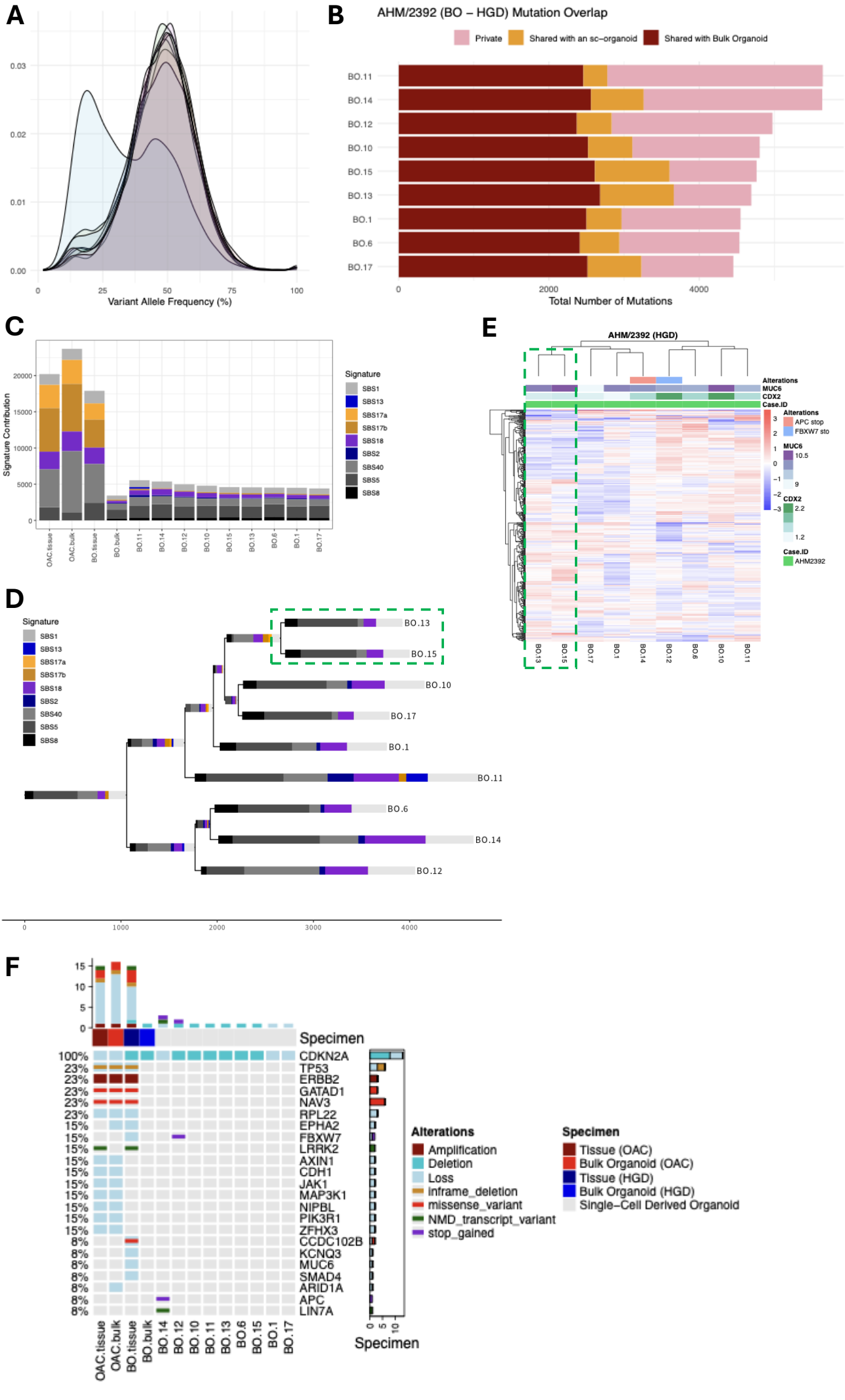

Supplementary Figure 5

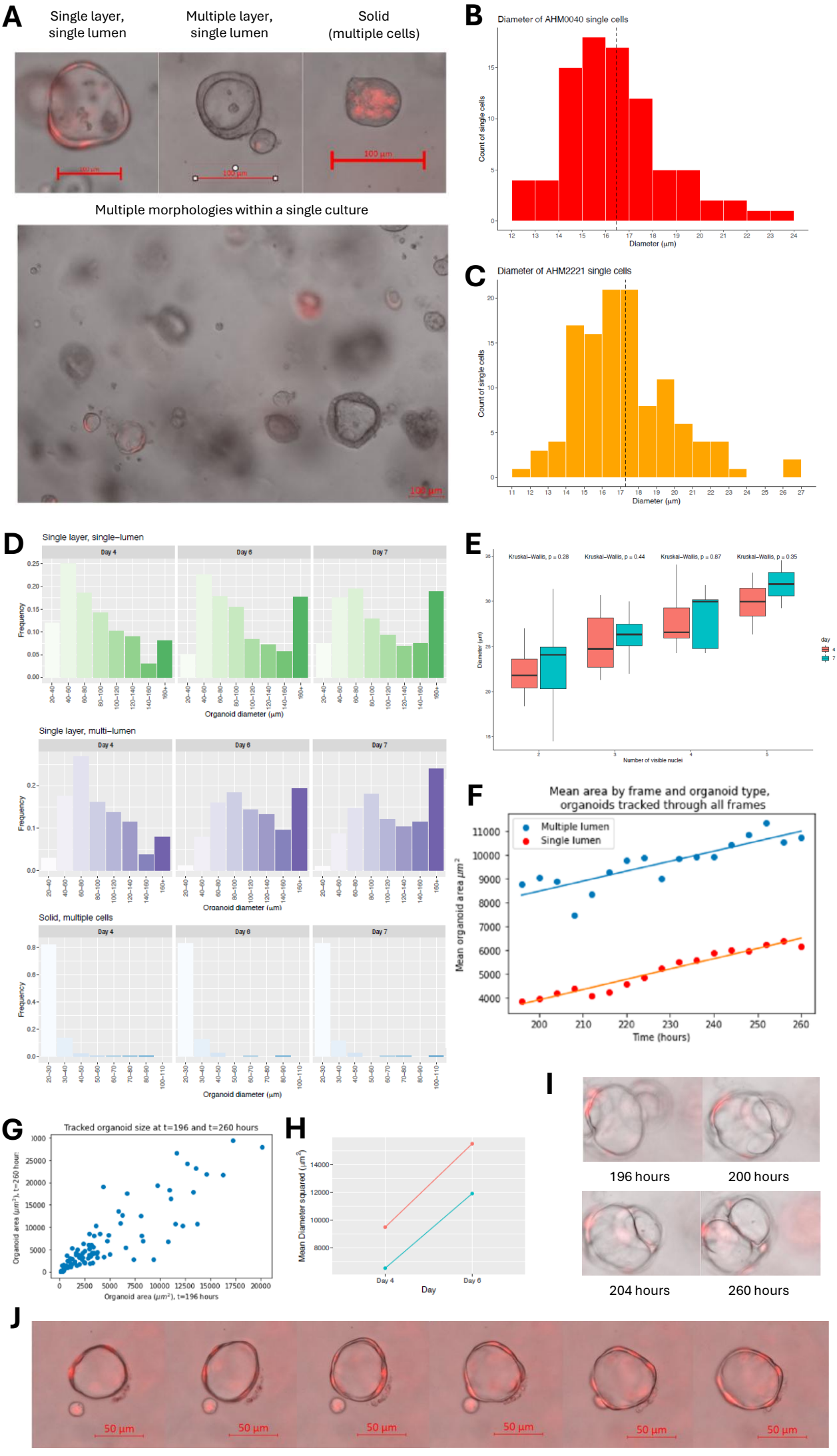

Supplementary Figure 6

A

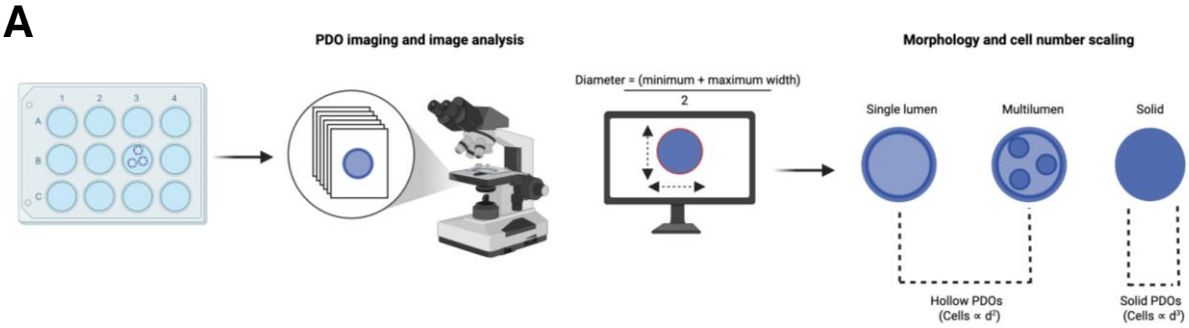

B

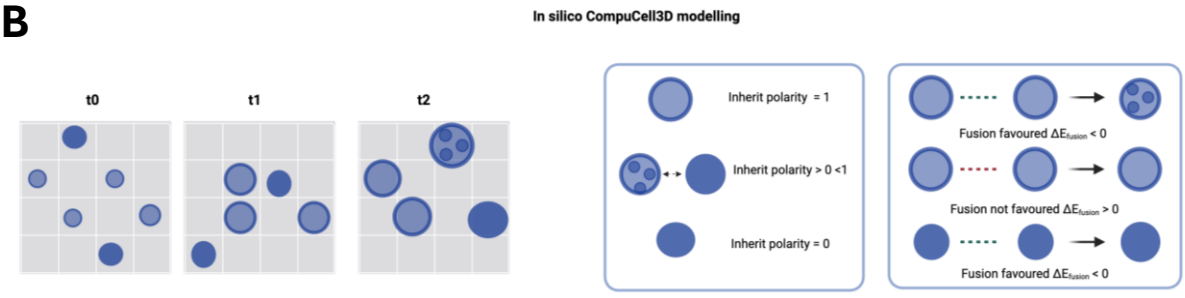

C

i

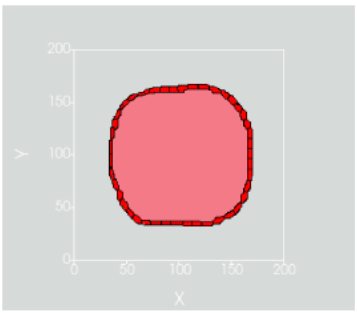

ii

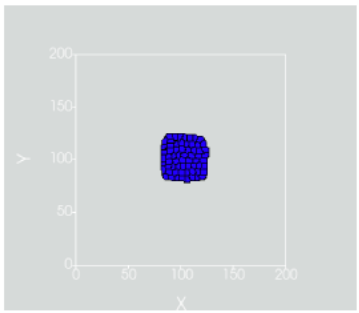

D

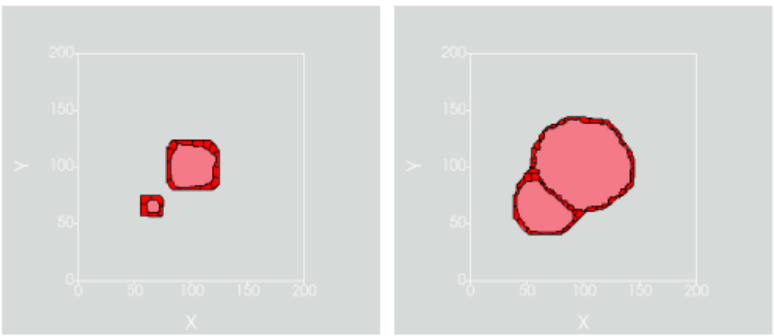

E

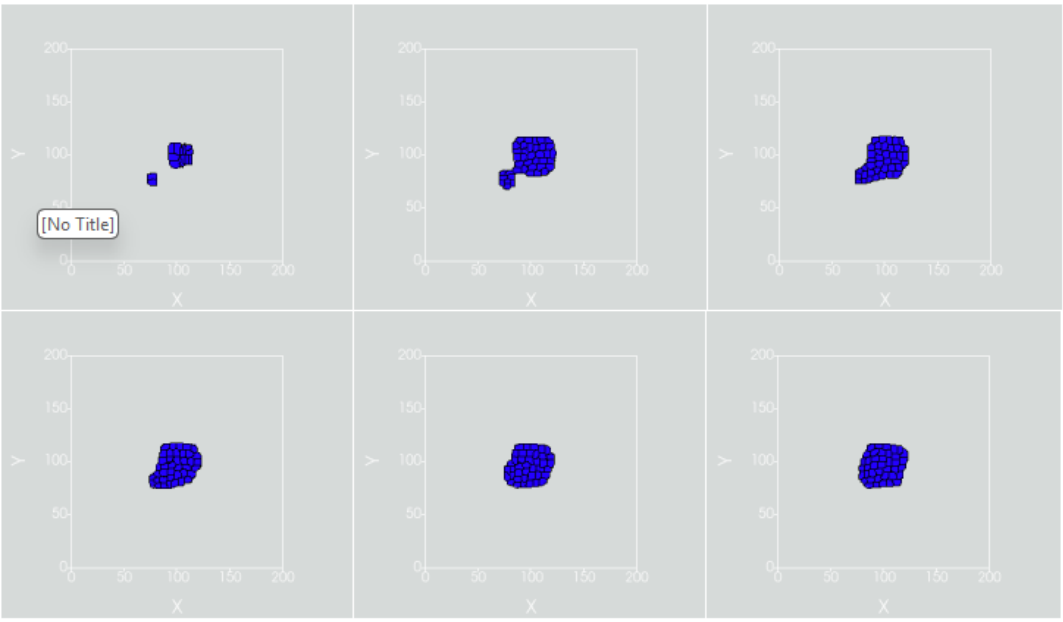

Supplementary Figure 7

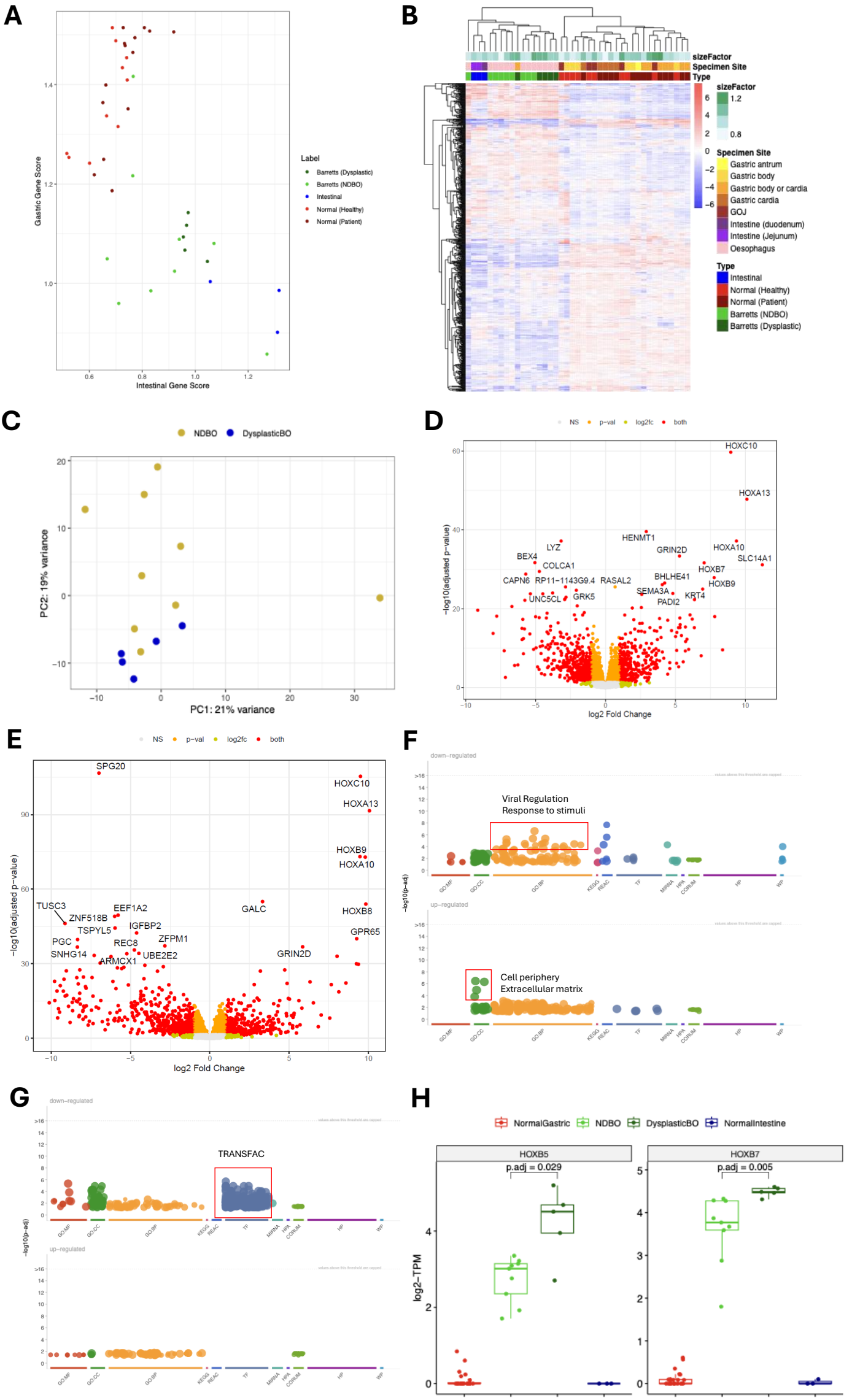

Supplementary Figure 8

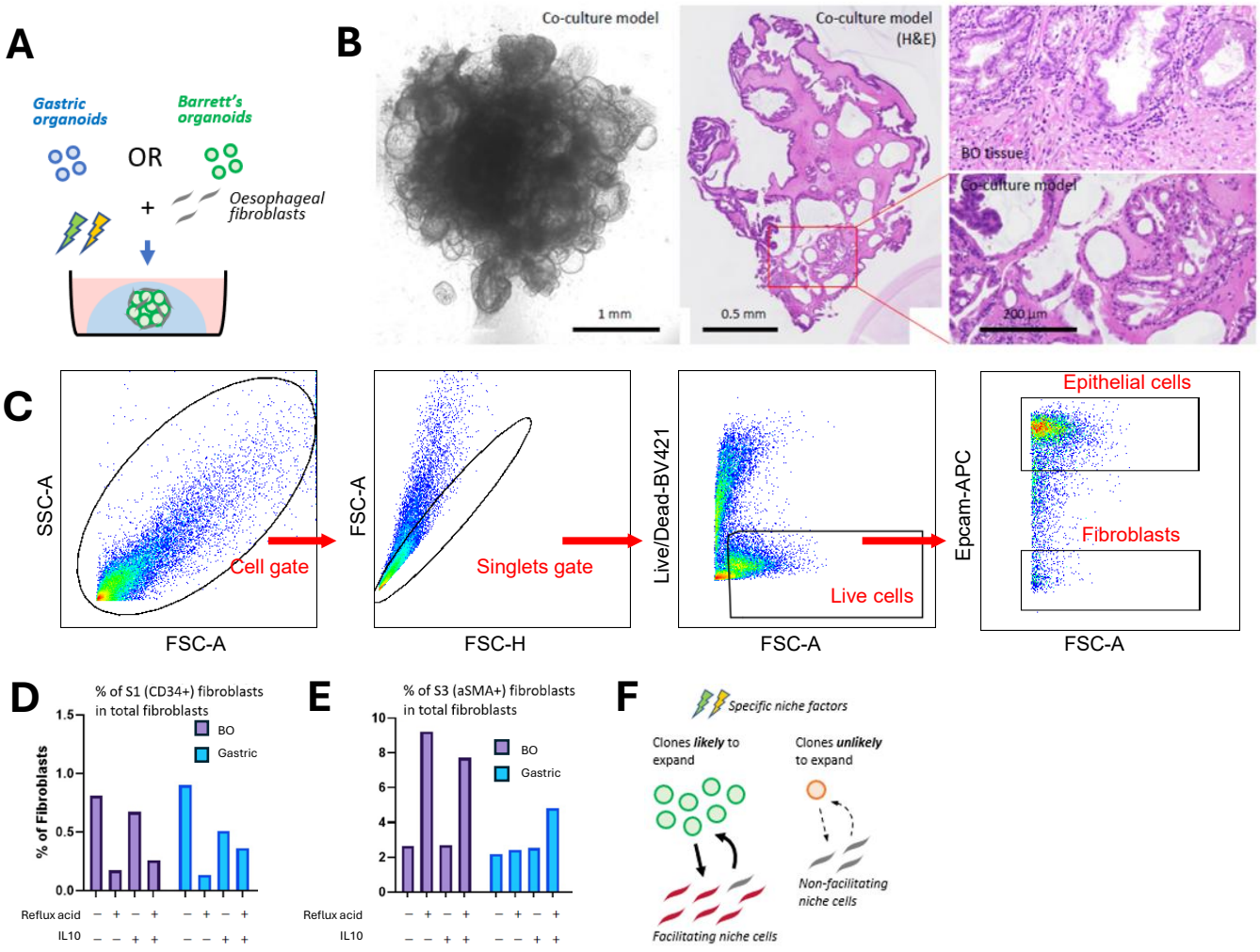

Supplementary Figure 9

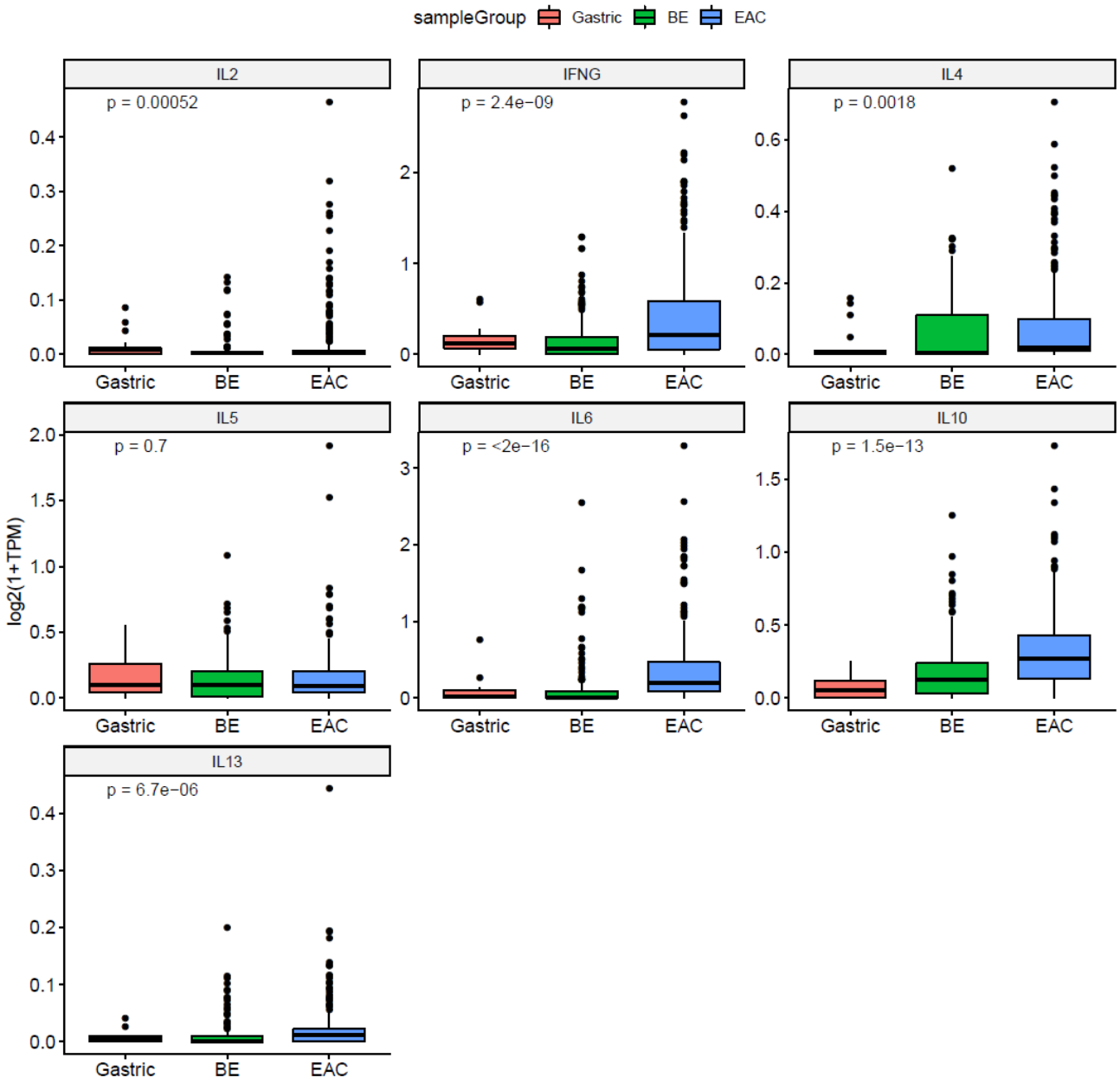

Supplementary Figure 10

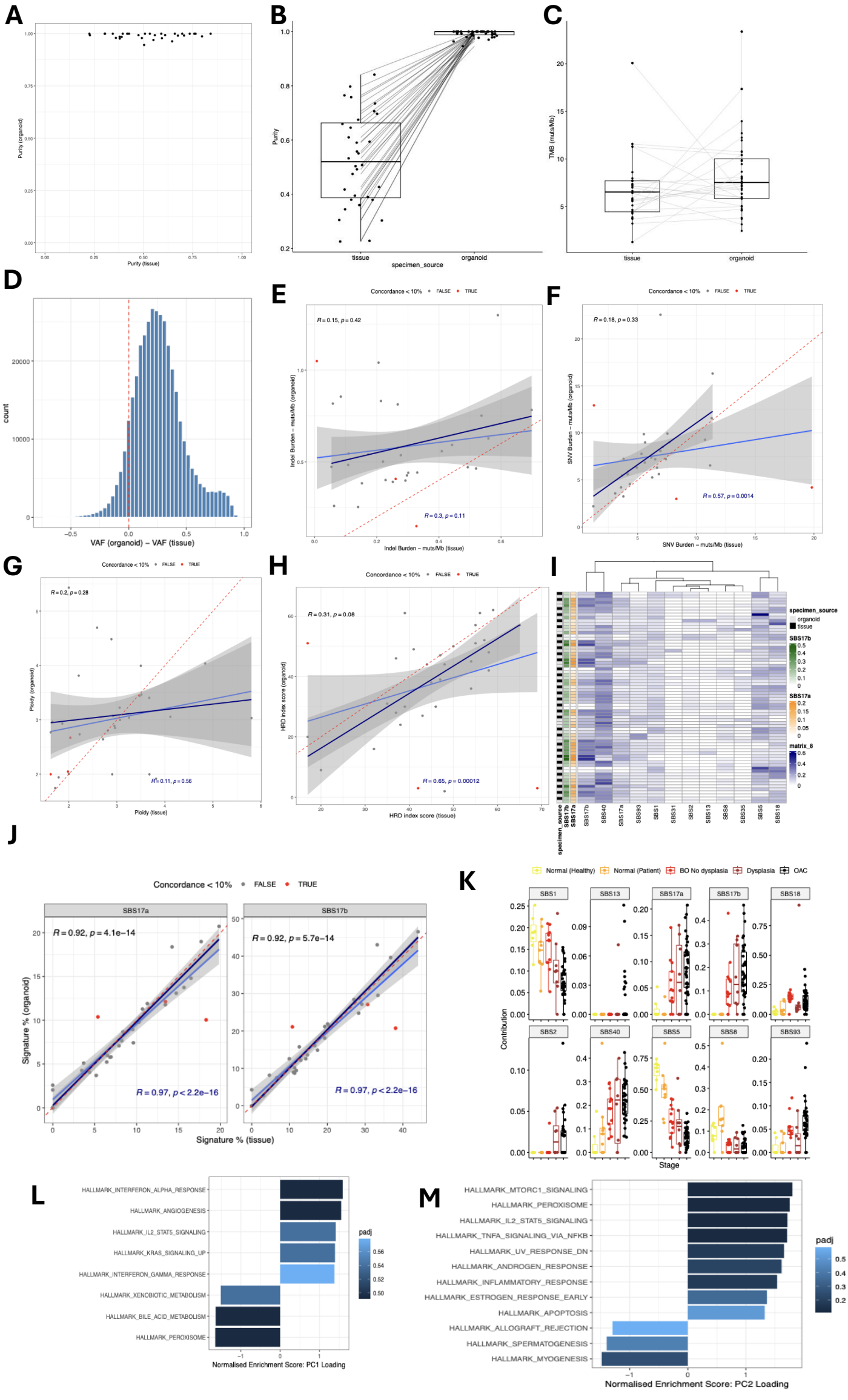

Supplementary Figure 11

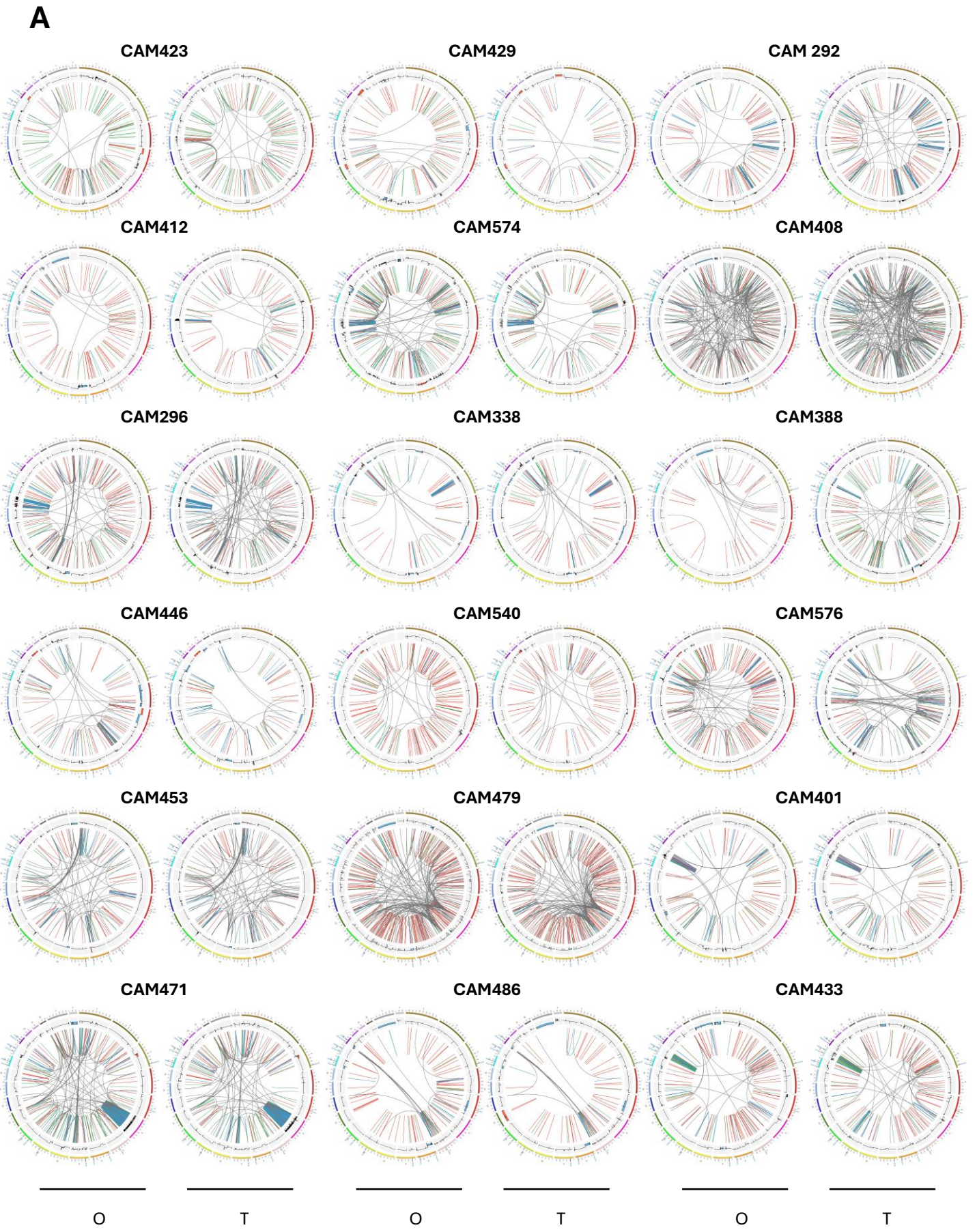

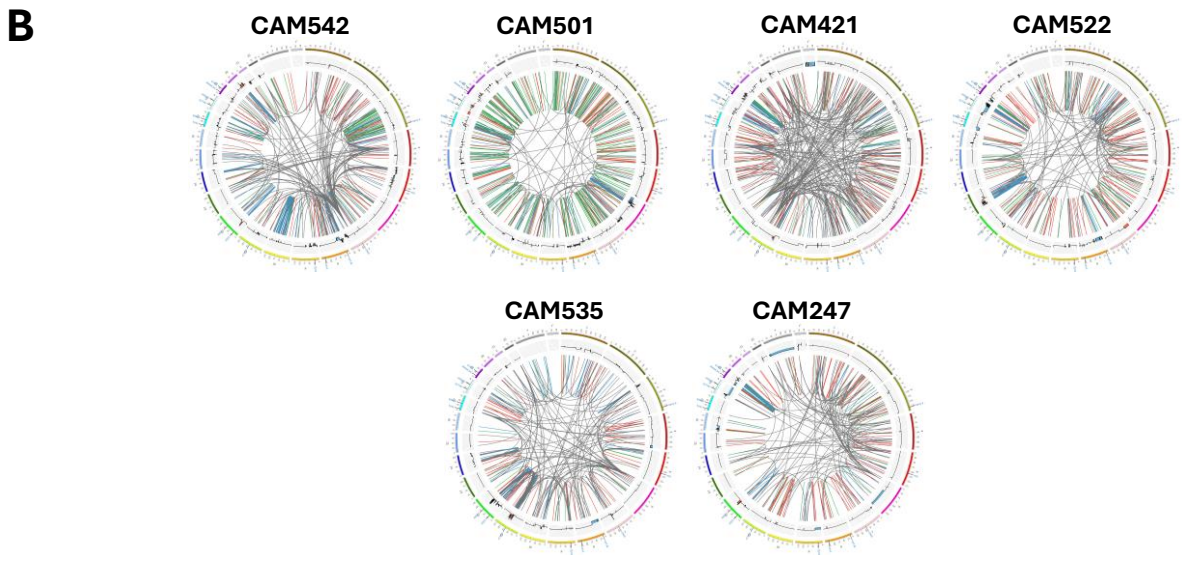

Supplementary Figure 12

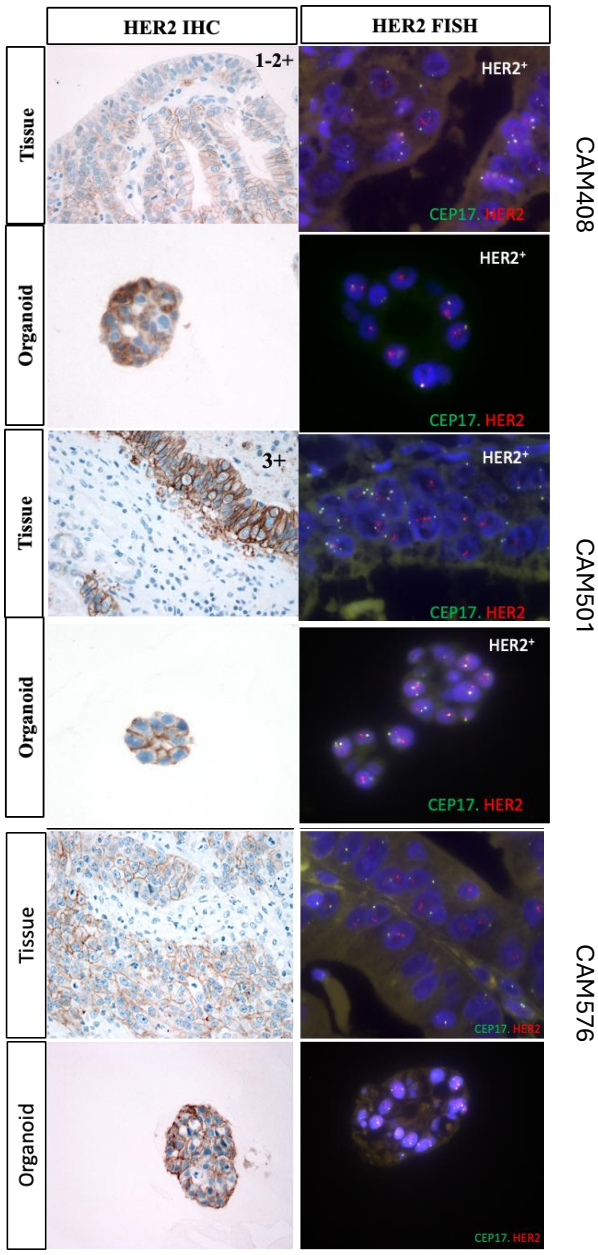

Supplementary Figure 13

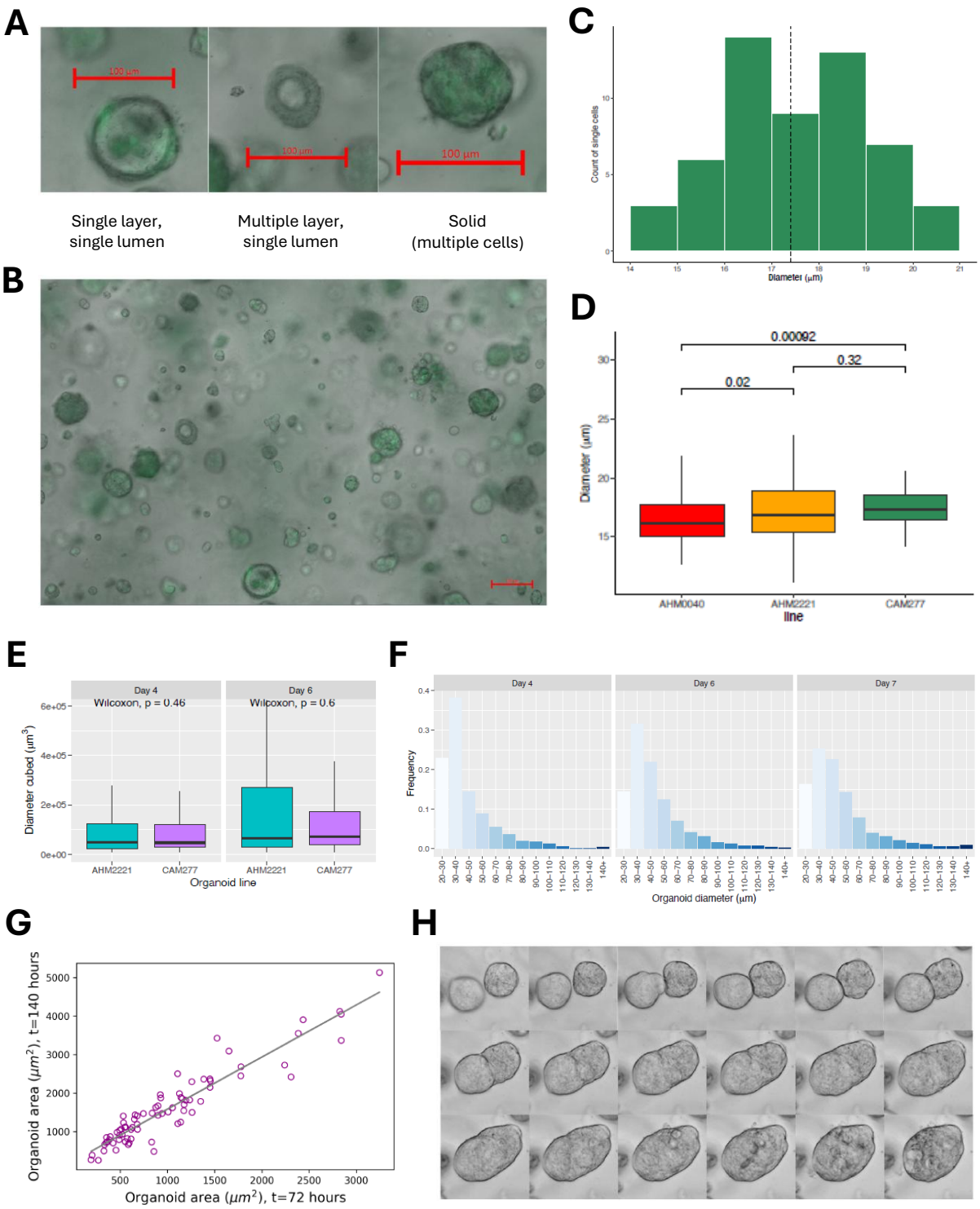
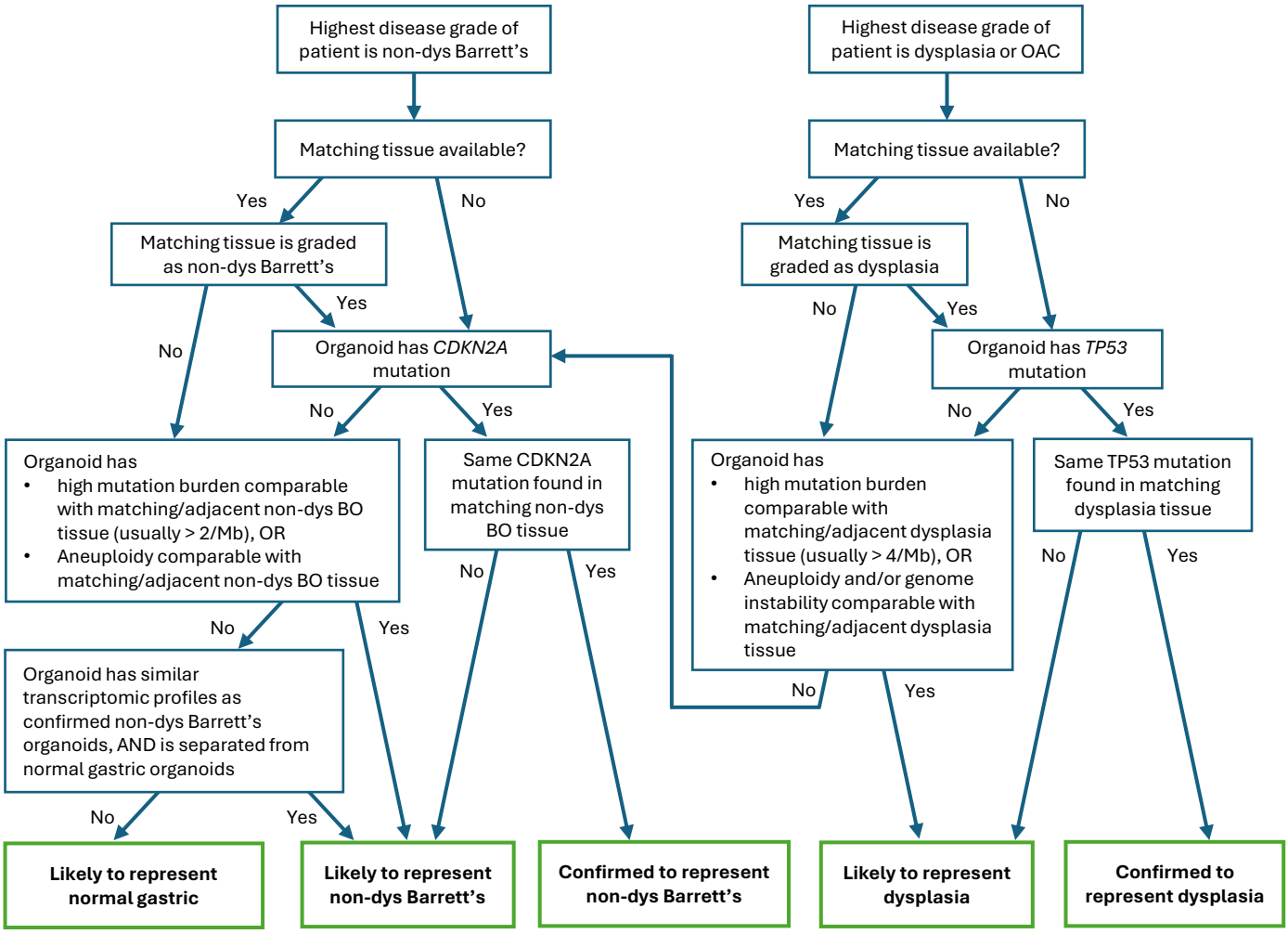
Supplementary Figure 14